

Barnabás PIRI

Students' Scientific Conference



Budapest University of Technology and Economics
Department of Applied Mechanics



**Experimental and numerical characterization of
critical parameters in elliptical shell snap-through**

Author:

Barnabás PIRI

Supervisor:

Dr. Szabolcs BEREZVAI, Assistant Professor

Students' Scientific Conference

Budapest, 2023

Acknowledgements

First and foremost, I would like to express my deepest appreciation to my supervisor, Dr. Szabolcs Berezvai (Department of Applied Mechanics), for his insightful comments and suggestions at every stage of my work.

I'm truly blessed to have such wonderful family and friends who have always stood by me and given me tremendous motivation even in the most difficult times.

This research has been supported by the Hungarian Scientific Research Fund, Hungary (under Contract: OTKA, PD 137806) and by the ÚNKP-23-2-I-BME-94 New National Excellence Program of the Ministry for Culture and Innovation from the source of the National Research, Development and Innovation Fund. These supports are gratefully acknowledged.



MINISTRY OF CULTURE
AND INNOVATION



NATIONAL RESEARCH, DEVELOPMENT
AND INNOVATION OFFICE
HUNGARY



NEW NATIONAL
EXCELLENCE PROGRAM

Budapest, 31 October 2023

Barnabás Piri

Contents

1	Introduction	1
1.1	Aim of the work	1
1.2	Layout	2
1.3	Nomenclature	3
2	Theoretical background	5
2.1	Hyperelastic material models	5
2.1.1	Strain measures	5
2.1.2	Concept of stress	7
2.1.3	Theory of hyperelasticity	8
2.1.4	The Ogden hyperelastic model	9
2.2	The snap-through phenomena	10
2.2.1	Fields of application	11
3	Preliminary research	15
3.1	The proposed geometry	15
3.2	Finite element modelling	16
3.2.1	General overview of the model	16
3.2.2	Automatic simulation environment	17
4	Experimental testing	19
4.1	Overview of the test setup	19
4.1.1	The fluidic control board	19
4.1.2	The measurement container	21
4.1.3	Specimen fabrication	22
4.1.4	Determination of the material parameters	25
4.2	Controlling the measurement board	27
4.2.1	Volume and pressure control	27
4.2.2	The PID controller	28
4.3	Measurement test procedure	30

5	Analytical modelling	31
5.1	Shell theory for circular shells	31
5.2	Proposed method for elliptical shells	33
6	Comparison and conclusion	35
6.1	Comparison of the presented methods	35
6.1.1	Results of the simulations	35
6.1.2	Results of the measurements	36
6.1.3	The analytical calculations	39
6.2	Conclusions	41
7	Summary	43
7.1	Summary of the paper	43
7.2.	A dolgozat összefoglalója	44
	References	47
	Appendix	49
A	The geometric description for FE models	49
B	Finite element modelling	55
B.1	Mesh independence study	55
B.2	Deformation of the measurement container	56
C	Characteristic of the used diaphragm pump	57
D	Optimization script for the equivalent circle	59

1

Introduction

1.1 Aim of the work

Soft materials have many engineering applications due to their favourable mechanical properties like flexibility, energy absorption, not to mention that they are easy to manufacture, with a low cost of prototyping. These characteristics make such materials the perfect basis for the design of complex mechanical systems, addressed as soft robotics [1, 2]. However, describing the exact behaviour of these materials is a complex task, as they exhibit nonlinear stress-strain characteristics, which is often paired with nonlinear geometric and loading conditions. By exploiting the unstable configurations of these hyperelastic materials, the response of the fluidic actuators applied in soft robotics can be enhanced. A general method for determining such characteristic of a shell is to find the appropriate load-displacement relationship, which can be done by resolving the pressure and volume relation of a closed cavity formed by the shell.

The aim of this contribution is to investigate the snap-through instability of soft elliptical shells and analyse the critical values which determines the main characteristics of the phenomena. The paper provides three methods to characterize the shells response to external loading cases. During my previous research, I developed a simulation environment capable of analysing the phenomena. After this, I carried out measurements corresponding to the FE calculations, which were performed using a self-developed fluidic control board, which provides the possibility to apply different loading- and control options [3]. The final approach is to determine the critical buckling pressure of the shells by analytical calculations, which is based on the basic principles of the description of the snap-through problem, which were first proposed by Zoelly [4].

After the methods has been presented, I will compare them qualitatively and quantitatively as well. The methodology of the paper can be summarized below.

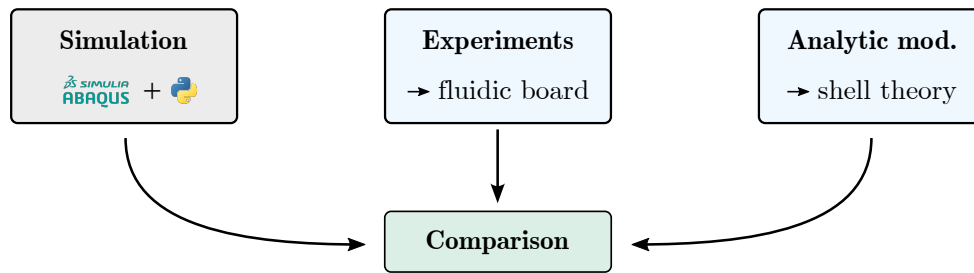


Figure 1.1: The methodology of the work

1.2 Layout

This thesis is divided into seven main chapters, including *Chapter 1*, where the goals and the structure of the thesis are presented.

Chapter 2 contains the basics of continuum mechanics, which is necessary to understand the used hyperelastic material models, and the snap-through phenomena. This chapter also contains some applications of the snap-through.

Chapter 3 is dedicated to summarize the prior research methodologies and objectives. This section provides the description of used geometry and the simulation environment.

Chapter 4 presents the development and the operation of the fluidic control board, which is dedicated to carry out the measurements.

Chapter 5 provides the description of the analytic theory of the snap-through phenomena and its application to the proposed geometry.

Chapter 6 is focused on comparing the different calculations (analytical and numerical) with the measurement results, which were conducted on three specimens.

In the end, *Chapter 7* contains the summary of my work in English and in Hungarian as well.

1.3 Nomenclature

If \mathbf{a} and \mathbf{b} are vectors, \mathbf{A} and \mathbf{B} are second order tensors and D is a scalar field quantity, the mathematical operations are interpreted as follows:

\mathbf{A}^T	Transpose of \mathbf{A}
\mathbf{A}^{-1}	Inverse of \mathbf{A}
$\dot{\mathbf{A}}$	Time derivative of \mathbf{A}
$\text{grad}(D)$	Gradient of D
$\det(\mathbf{A})$	Determinant of \mathbf{A}
$\mathbf{a} \otimes \mathbf{b}$	Dyadic product between \mathbf{a} and \mathbf{b}
$\mathbf{A} : \mathbf{B}$	Double dot product between \mathbf{A} and \mathbf{B} , ($\mathbf{A} : \mathbf{B} = A_{ij}B_{ij}$)

Important characters are summarized below:

\mathbf{X}	Referential position
\mathbf{x}	Current position
\mathbf{E}_i	Unit basis vectors in the reference configuration
\mathbf{e}_i	Unit basis vectors in the spatial configuration
ϕ	General mapping
\mathbf{F}	Deformation gradient
J	Volume ratio
\mathbf{C}	Right Cauchy - Green deformation tensor
\mathbf{b}	Left Cauchy - Green deformation tensor
\mathbf{U}	Right stretch tensor
\mathbf{V}	Left stretch tensor
\mathbf{R}	Proper orthogonal tensor
\mathbf{t}	Cauchy traction vector
\mathbf{T}	First Piola - Kirchhoff traction vector
\mathbf{N}	Unit normal of the surface element in the reference configuration
\mathbf{n}	Unit normal of the surface element in the spatial configuration
$\boldsymbol{\sigma}$	Symmetric Cauchy stress tensor
\mathbf{P}	First Piola - Kirchhoff stress tensor
$\boldsymbol{\tau}$	Kirchhoff stress tensor
W	Stored strain energy per unit reference volume
λ_i	Eigenvalues of \mathbf{U} or \mathbf{V}
μ_k, α_k	Parameters of the Ogden hyperelastic model

q	Intensity of distributed load
A_i, B_i, θ_i, t_i	Parameters of the ellipse
R, θ_{ic}	Radius and opening angle of the equivalent circle
P_{cr}^s	Critical pressure from simulation
P_{cr}^{mv}	Critical pressure from volume controlled measurements
P_{cr}^{mp}	Critical pressure from pressure controlled measurements
P_{cr}^a	Critical pressure from analytic calculation
P_{cr}^e	Critical pressure from empiric relation

2

Theoretical background

2.1 Hyperelastic material models

2.1.1 Strain measures

In solid mechanics, the behavior of a deformable solid can be described using the phenomenological approach of continuum mechanics. Continuum theory assumes that we are concerned with a body in which both mass and volume are continuous functions of continuum particles [5, 6]. A general motion of a continuum body is shown in Fig. 2.1 below.

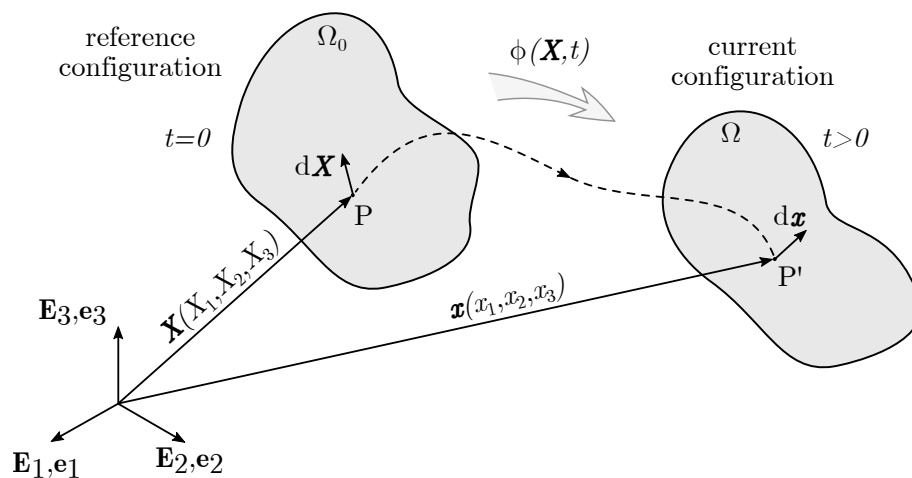


Figure 2.1: Representation of a continuum body

The body in its initial position occupies the region Ω_0 in which the material points are identified with their coordinates \mathbf{X} with respect to the Cartesian basis \mathbf{E}_i . This configuration is referred as the reference configuration [5, 6]. After the deformation, the current position of material points can be described with the vector \mathbf{x} in the basis \mathbf{e}_i , which is called current configuration. Between these configurations, a unique mapping can be defined as

$$\mathbf{x} = \phi(\mathbf{X}, t). \quad (2.1)$$

Assuming the motion to be uniquely invertible, the inverse of the mapping is

$$\mathbf{X} = \phi^{-1}(\mathbf{x}, t). \quad (2.2)$$

In continuum mechanics, we distinguish between two ways of description. In the Lagrangian (or material) description, the quantities are characterized with respect to the reference configuration, meanwhile, the Eulerian (or spatial) description uses the current configuration to identify the quantities [6]. A primary measure of deformation can be introduced as

$$\mathbf{F}(\mathbf{X}, t) = \frac{\partial \phi(\mathbf{X}, t)}{\partial \mathbf{X}}, \quad (2.3)$$

known as the deformation gradient, which must satisfy $\det(\mathbf{F}) > 0$, to ensure non-singular motion. This gradient can be used to form a relationship between the infinitesimal line and volume elements as

$$d\mathbf{x} = \mathbf{F} d\mathbf{X} \quad \text{and} \quad dv = J dV, \quad (2.4)$$

where $J = \det(\mathbf{F})$ is the volume ratio. Using the deformation gradient, several strain measures can be introduced, starting with the right and the left Cauchy–Green deformation tensors defined as

$$\mathbf{C}(\mathbf{X}, t) = \mathbf{F}^T \mathbf{F}, \quad (2.5)$$

$$\mathbf{b}(\mathbf{X}, t) = \mathbf{F} \mathbf{F}^T. \quad (2.6)$$

The deformation gradient can be decomposed in a form

$$\mathbf{F} = \mathbf{R} \mathbf{U} = \mathbf{V} \mathbf{R}, \quad (2.7)$$

using the polar decomposition theorem, where $\mathbf{U}(\mathbf{X}, t)$ is the right, $\mathbf{V}(\mathbf{X}, t)$ is the left stretch tensor, and \mathbf{R} is an orthogonal rotation tensor [6]. The stretch tensors are related to the strain tensors as

$$\mathbf{U} = \sqrt{\mathbf{C}} \quad \text{and} \quad \mathbf{V} = \sqrt{\mathbf{b}}. \quad (2.8)$$

The λ_i eigenvalues of \mathbf{U} and \mathbf{V} are called principal stretches, while the corresponding normalized eigenvectors define the principal directions. The principal stretches give the ratio between the current and the initial length of a deformed line element oriented in the principal direction [5, 6, 7].

2.1.2 Concept of stress

Motion and deformation give rise to interactions between the continuum body and its neighboring environment. One consequence of these interactions is stress, which is a representation of the internal forces acting on a unit surface area. The mathematical description can be introduced using Fig. 2.2, which shows a deformable continuum body, occupying the region Ω with boundary surface $\partial\Omega$. Let the body be cut by a surface that passes through any given point $\mathbf{x} \in \Omega$, thus separating the body into two portions [5, 6]. The forces are transmitted across a planar surface. The force acting on the infinitesimal surface area is denoted by $d\mathbf{f}$, and it can be defined for every element as

$$d\mathbf{f} = \mathbf{t}ds = \mathbf{T}d\mathbf{S}, \quad (2.9)$$

where $\mathbf{t}(\mathbf{x}, t, \mathbf{n})$ represent the Cauchy traction vector, while $\mathbf{T}(\mathbf{X}, t, \mathbf{N})$ is the first Piola–Kirchhoff traction vector. The infinitesimal surface elements are defined with their normal vectors (facing outwards) \mathbf{n} and \mathbf{N} , respectively. Cauchy’s stress theorem states, that

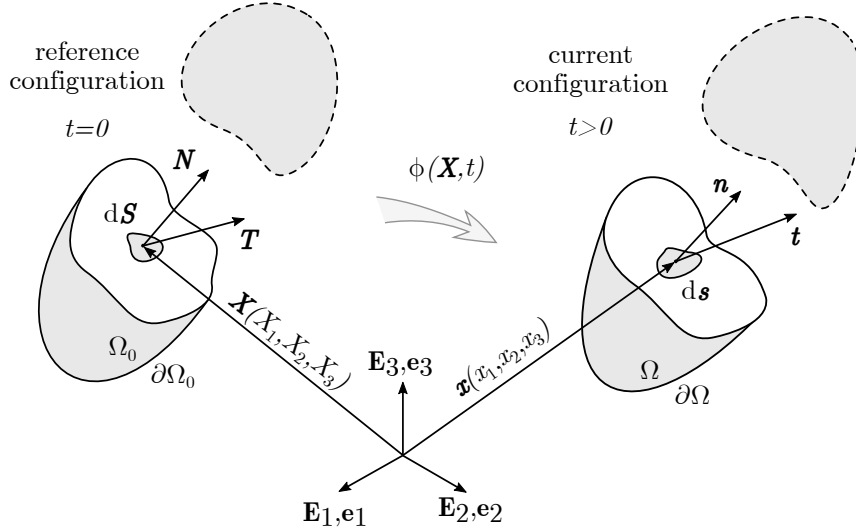


Figure 2.2: Traction vectors acting on the infinitesimal surface elements

there exist some unique second - order tensor fields $\boldsymbol{\sigma}$ and \mathbf{P} such that the traction vectors can be expressed as

$$\mathbf{t}(\mathbf{x}, t, \mathbf{n}) = \boldsymbol{\sigma}(\mathbf{x}, t) \mathbf{n}, \quad (2.10)$$

$$\mathbf{T}(\mathbf{X}, t, \mathbf{N}) = \mathbf{P}(\mathbf{X}, t) \mathbf{N}, \quad (2.11)$$

where $\boldsymbol{\sigma}$ is the symmetric, so-called Cauchy stress tensor, and \mathbf{P} is the first Piola–Kirchhoff stress tensor [6]. The Cauchy stress tensor can be expressed with the first Piola–Kirchhoff stress tensor as

$$\boldsymbol{\sigma} = J^{-1} \mathbf{P} \mathbf{F}^T. \quad (2.12)$$

From the Cauchy stress tensor, the Kirchhoff stress tensor can be introduced as

$$\boldsymbol{\tau} = J \boldsymbol{\sigma}. \quad (2.13)$$

2.1.3 Theory of hyperelasticity

Small-strain theory is a mathematical approach to describe the deformation of a solid body, in which the displacements of the material particles are assumed to be much smaller than any relevant dimension of the body. For materials like soft rubbers, stress-strain relations cannot be described using this approach, because these materials are capable of high deformations, while maintaining material continuity [6]. As a consequence of this, to describe the mechanical behavior, we need to use the so-called (finite) hyperelasticity theory, which postulates the existence of a strain energy function $W = W(\mathbf{F})$, which is an explicit function of the deformation gradient \mathbf{F} . This strain energy function is a polyconvex function, which is expressing the stored strain energy per unit reference volume. Since it's only a function of the deformation gradient, this postulates that we are dealing with homogeneous materials, in which the distribution of internal constituents are assumed to be uniform on the continuum scale [6, 7]. The theory states, that the stress power per unit reference volume is equal to the time derivative of the strain energy function. The stress power is also related to stress tensors as

$$\dot{W} = J \boldsymbol{\sigma} : \mathbf{d} = \boldsymbol{\tau} : \mathbf{d} = \mathbf{P} : \dot{\mathbf{F}}. \quad (2.14)$$

At the same time, we can express this quantity as the time-derivative of the strain energy function by using the chain rule of derivation:

$$\dot{W} = \frac{\partial W(\mathbf{F})}{\partial \mathbf{F}} : \dot{\mathbf{F}}. \quad (2.15)$$

Comparing Eq. (2.14) with Eq. (2.15), we can express the first Piola–Kirchhoff stress tensor as an explicit function of the strain energy as

$$\mathbf{P} = \frac{\partial W(\mathbf{F})}{\partial \mathbf{F}}. \quad (2.16)$$

If the continuum body is subjected to rigid-body rotation, the strain energy function cannot change because of material objectivity, mathematically expressed as

$$W(\mathbf{F}) = W(\mathbf{Q} \mathbf{F}). \quad (2.17)$$

If the rigid-body rotation is chosen as $\mathbf{Q} = \mathbf{R}^T$ based on the polar decomposition theorem, W can be expressed as a function of the right stretch tensor as

$$W(\mathbf{F}) = W(\mathbf{Q} \mathbf{F}) = W(\mathbf{Q} \mathbf{R} \mathbf{U}) = W(\mathbf{R}^T \mathbf{R} \mathbf{U}) = W(\mathbf{U}), \quad (2.18)$$

which is now can be related to the right Cauchy–Green deformation tensor using Eq. (2.8), so the strain energy is given by a function

$$W(\mathbf{F}) = \tilde{W}(\mathbf{C}). \quad (2.19)$$

Now, the time-derivative of the strain energy function can be expressed in terms of the right Cauchy–Green deformation tensor as

$$\dot{W} = \frac{\partial W(\mathbf{F})}{\partial \mathbf{F}} : \dot{\mathbf{F}} = \frac{\partial \tilde{W}(\mathbf{C})}{\partial \mathbf{C}} \frac{\partial \mathbf{C}}{\partial \mathbf{F}} : \dot{\mathbf{F}}. \quad (2.20)$$

Comparing the formulations of Eq. (2.15) with Eq. (2.20), we can conclude that the first Piola–Kirchhoff stress tensor can be written as the explicit function of the right Cauchy–Green deformation tensor:

$$\mathbf{P} = 2\mathbf{F} \frac{\partial W(\mathbf{C})}{\partial \mathbf{C}}. \quad (2.21)$$

Applying the relation between the stress tensors expressed in Eq. (2.12), the Cauchy stress tensor can be written as

$$\boldsymbol{\sigma} = \frac{2}{J} \mathbf{F} \frac{\partial W(\mathbf{C})}{\partial \mathbf{C}} \mathbf{F}^T. \quad (2.22)$$

The representation theorem for invariants states, that if a scalar-valued tensor function is an invariant under a rotation, it can be expressed in terms of the principal invariants of its argument [5, 6, 7]. In our case, we have the scalar function W which has the argument \mathbf{C} (right Cauchy–Green deformation tensor) or \mathbf{b} (left Cauchy–Green deformation tensor), hence

$$W = W(I_1, I_2, I_3), \quad (2.23)$$

where $I_i = I_i(\mathbf{C}) = I_i(\mathbf{b})$ are the principal invariants of \mathbf{C} or \mathbf{b} . Similarly, we can express the strain energy function in terms of the principal stretches λ_i , since they are the eigenvalues of the stretch tensors:

$$W = W(\lambda_1, \lambda_2, \lambda_3). \quad (2.24)$$

Using this formulation of the strain energy function, and substituting back into Eq. (2.22) we can derive an equation that gives the relation between the principal stretches and the stress tensor, expressed as

$$\boldsymbol{\sigma} = \sum_{k=1}^3 \frac{\lambda_k}{J} \frac{\partial W}{\partial \lambda_k} \mathbf{n}_k \otimes \mathbf{n}_k, \quad (2.25)$$

where \mathbf{n}_k are the unit eigenvectors of the left Cauchy–Green deformation tensor \mathbf{b} [5].

2.1.4 The Ogden hyperelastic model

There are plenty of hyperelastic models available in finite element software to simulate the response of rubbery materials. One of the most common hyperelastic model was developed by Ogden in 1972, which has multiple formulations [6, 7]. The strain energy function is expressed in terms of the principal stretches. In ABAQUS the strain energy function is defined as

$$W(\bar{\lambda}_1, \bar{\lambda}_2, \bar{\lambda}_3) = \sum_{k=1}^N \frac{2\mu_k}{\alpha_k^2} (\bar{\lambda}_1^{\alpha_k} + \bar{\lambda}_2^{\alpha_k} + \bar{\lambda}_3^{\alpha_k} - 3) + \sum_{k=1}^N \frac{1}{D_k} (J - 1)^{2k}, \quad (2.26)$$

where $\bar{\lambda}_i = J^{-\frac{1}{3}} \lambda_i$ and N is the order of hyperelastic the model. The parameters α_k , μ_k and D_k are material properties [8]. The volumetric response of the material is written in terms of the D_k parameters. During my work, I used incompressible materials (see Section 4.1.4 for specifications), where the volume ratio $J = 1$, meaning that the strain energy function can be simplified as

$$W(\lambda_1, \lambda_2, \lambda_3) = \sum_{k=1}^N \frac{2\mu_k}{\alpha_k^2} (\lambda_1^{\alpha_k} + \lambda_2^{\alpha_k} + \lambda_3^{\alpha_k} - 3). \quad (2.27)$$

The material's initial shear modulus μ_0 can be calculated from the μ_i parameters as

$$\mu_0 = \sum_{k=1}^N \mu_k > 0. \quad (2.28)$$

It is important to note, that the formulation which is present in ABAQUS is only valid for $\mu_k > 0$, however the nonlinearity parameter α can be either negative or positive [8].

2.2 The snap-through phenomena

Most elastic structures have several possible equilibrium states, which can be stable or unstable. The transformation from one state (often) happens via a rapid motion, which is called snap-through. This happens because we are building up elastic energy inside the structure, which releases suddenly, which generates rapid motions. Essentially, the effect of snap-through is a special case of buckling, which is usually a very dangerous failure mode of structural systems. Buckling happens, when a structure is subjected to a gradually increasing load, which eventually exceeds a critical level, the structure releases a sudden burst of energy and deforms to another stable state [9, 10, 11, 12].

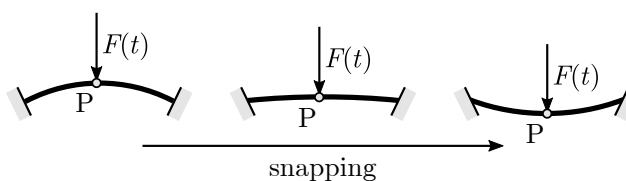


Figure 2.3: A simple example of the snap-through

The phenomena can be characterized by the force-displacement relationship, which is highly nonlinear. A general equilibrium path of a system seen on Fig. 2.4 is plotted below. However, if we conduct the experiments, we are unable to trace the whole curve, because some points on it are unstable configurations, which can't be reached in an experiment [6]. There are two control methods that can be used in an experiment: in the first method, we are controlling the input force, while in the other method, we are driving the displacement. These two approaches are illustrated on a general nonlinear behaviour on Fig. 2.5.

In finite element software, the load controlled method means that the load increment kept constant during an increment, conversely to the displacement control, when we keep

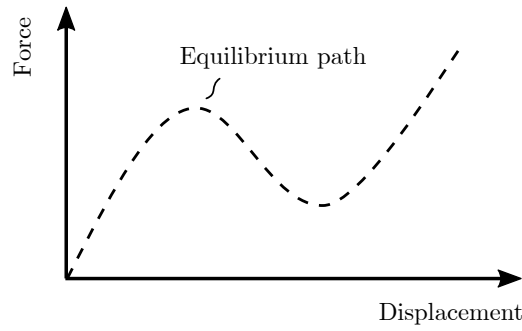


Figure 2.4: Equilibrium path of the arc's midpoint

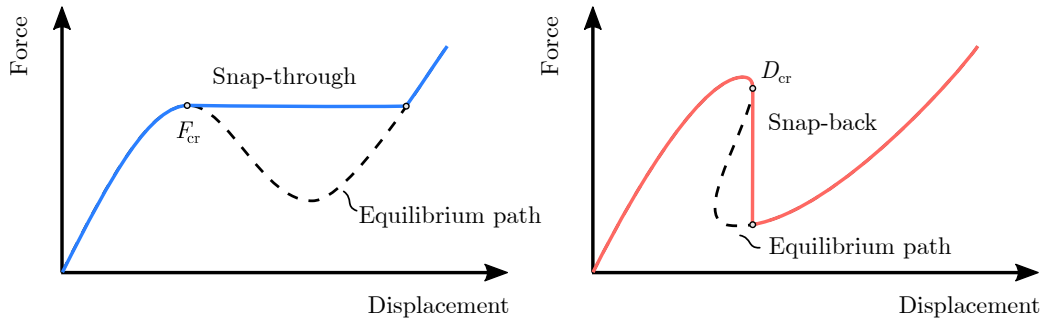


Figure 2.5: The snap-through and snap-back behaviour

the displacement constant during an increment [13, 14]. However, as we can see, they both fail at a critical point on the curve, we can be denoted by the critical force and critical displacement. By taking the advantageous numerical method first proposed by *Riks* (called arc-length method), we can solve these problems assuming quasi-static conditions, and finally we are able to trace the whole equilibrium path [13].

2.2.1 Fields of application

The snap-through phenomena has several applications in every field of engineering, but as my work involves in the study of soft (rubber-like, silicone) materials, I will focus on soft robotics [1, 15].

Xinjie Zhang et al. presented a soft valve, which takes advantage of the snapping of a silicone shell [16]. They proposed a design, which is suitable to control the flow in soft systems. It works very similarly to the principle that I am investigating: when the supply pressure of the system exceeds the critical pressure of the shell, it snaps to the other configuration, relieving the pressure of the system, thus keeping it safe.

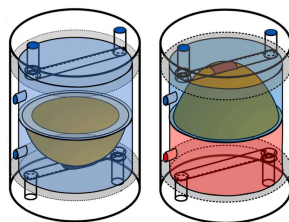


Figure 2.6: The original (left) and the invert (right) state [16]

The research group of *Yichao Tang* proposed several design principles of soft actuators, that are focused on speed / force by harnessing the mechanical instability of the silicone materials [11]. One of the actuators formed a bistable gripper, which can be seen on the Fig. 2.5. Thanks to the tendon inserted into the soft material, it can produce high grip forces, thus it can move weights heavier than 10 kg. However, when we are dealing with delicate materials (for example, consider an egg), then we can only actuate the pneumatic part of the gripper.

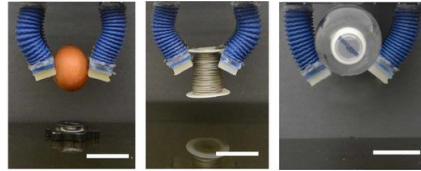


Figure 2.7: Bistable gripper with different weights [11]

Soft robotics plays an important role in biomedical applications as well, because the materials from which the actuators are made of are usually biocompatible. *E.B. van der Houwen et al.* analysed silicone shells from a shunt valve, which is routinely implanted in the neck region of the laryngectomy patient (whose larynx has been excised as a remedy against cancer of the throat) [17]. These patients can only speak by pushing the valve, thus pressing the exhaled air through the esophaegal tissue. The valve designed by the group is called a *handsfree speech valve*, because leveraging the bistable positions of the shell, they achieved that the patient doesn't need to hold the shell constantly: after pressing it snaps to the other stable state, and after pressing it again, it snaps back to the original state [17].

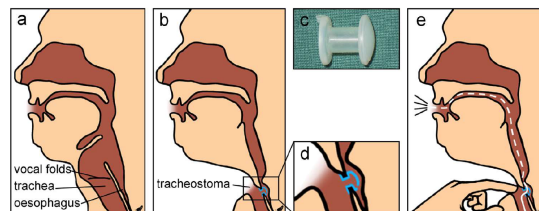


Figure 2.8: Laryngectomy patient with a shunt valve [17]

Another example can be given by the industry: the team of *Ying Lin* developed a pipe crawler robot [18]. The soft robot capable of moving through a pipe (even if it's filled with water) with a single actuation motion. In this study, they harnesses the highly nonlinear buckling of elastic ribbons and bioinspired artificial muscles to significantly enhance the crawling capability of previous designs.

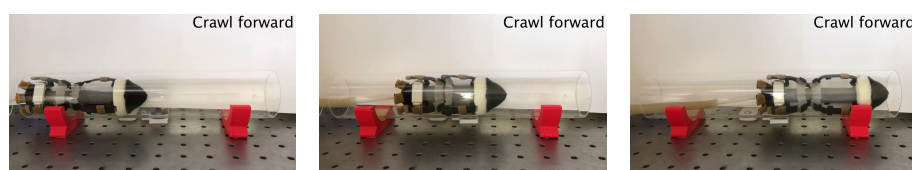


Figure 2.9: Single actuation pipe crawler [18]

After all, the list could be continued for several pages, which highlights the great need to understand the behaviour of these soft materials better. For a more in-depth review of the current state of the art, we could read the work of *Aniket Pal et al.* which summarizes several other concepts which were not introduced above [15].

3

Preliminary research

This chapter provides a short summary of my previous work in the topic. My paper presented at last year's conference was titled *Optimization of soft robots based on hyperelastic instabilities*, since in this work an FE-based optimization procedure was proposed. I successfully created an automatic simulation environment for a fluidic actuator, which was used to investigate the behaviour of the snap-through instability with different material and geometric properties.

3.1 The proposed geometry

The geometric design was inspired by the article *Inflatable soft jumper inspired by shell snapping* written by *Gorissen et al.* [19]. Their geometry consist of two spherical caps, which are joined together at their base. If the cavity between the two shells are inflated, the inner (lower) cap snaps to another stable state. I investigated a more general form of this geometry, replacing the inner spherical shell with general elliptical shell, which led to more distinguished geometric parameters and more possible combinations out of them. The figure of the proposed geometry can be seen of Fig. 3.1.

The geometry and the loading (and boundary) conditions is axisymmetric, and the material models reflex homogeneous isotropic material behaviour, the geometry can be analysed by axisymmetric models. This simplification ensures, that the models are simple enough (compared to a 3D solid model) to be able to analyse a lot of parameter combinations in a relatively short amount of time. Note, that the subscripts „*i*” and „*o*” indicate the quantities for the inner and outer shell, respectively.

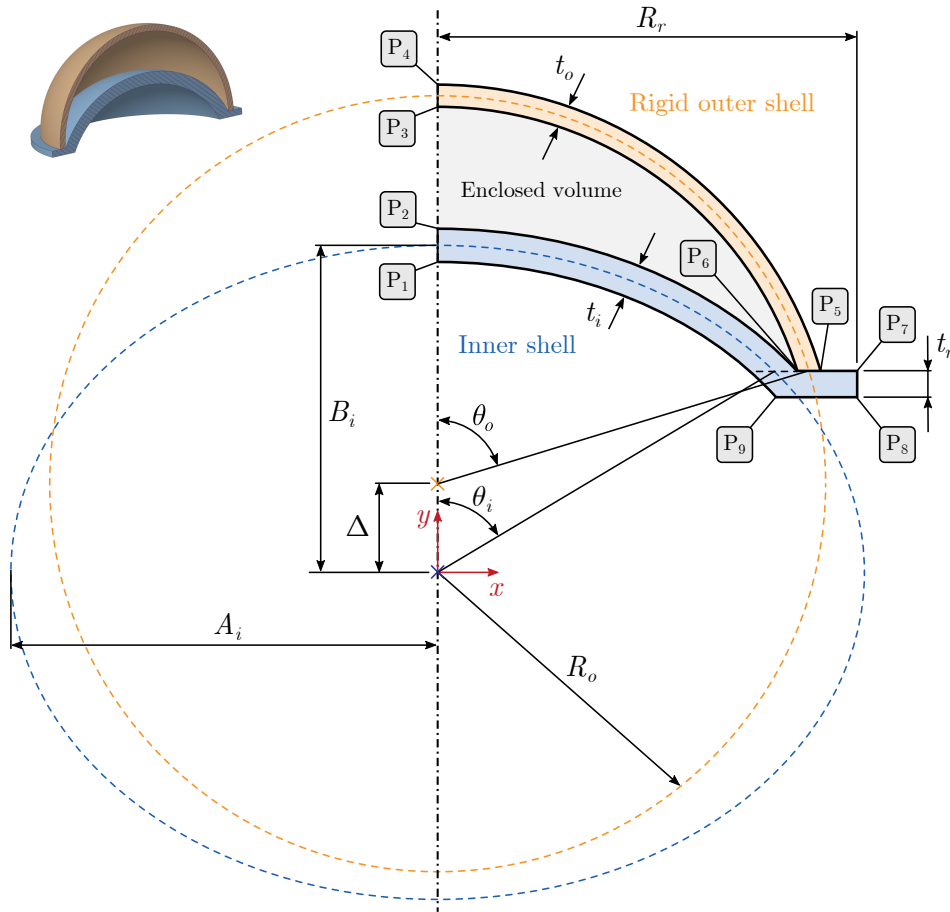


Figure 3.1: The geometry and its parameters

During my work I investigated only the behaviour of the snapping shell, which is in this case the inner shell. As a consequence of this, the outer shell is assumed as a completely rigid shell, thus when we are inflating the enclosed volume by a fluid, it won't deform. This property will be enhanced at [Section 4.1](#) to simplify the experimental setup.

The coordinates of the points listed in [Fig. 3.1](#) can be easily obtained, which were done previously, and can be seen in [Appendix A](#).

The conclusion is that the axisymmetric geometry is defined using 4 input parameters, which are used to describe the inner elliptical shell in its entirety. These parameters are the semi-axes (A_i and B_i), the opening angle (θ_i) and the shell's thickness (t_i).

3.2 Finite element modelling

3.2.1 General overview of the model

The simulations were done in the ABAQUS finite element software, which has a module called *Interaction*, in which the user can define interactions between regions of the model such as a contact. One of the interactions is the so-called *Fluid Cavity interaction*, which can be used to model fluid filled cavities. This tool is very useful, when the deformation of

the structure and the pressure of the contained fluid are not independent. These coupled problems can be solved by using a virtual cavity, which is defined by the surfaces of the enclosed volume, and a reference point, which defines the direction of the surface normals [8].

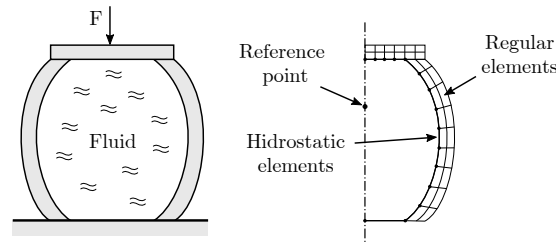


Figure 3.2: Discretization of a fluid-filled structure, redrawn as [8]

Regarding my model, the selection of these geometric parameters can be defined by Fig. 3.3, which shows a simplified FE model of the structure. Important to note, that the mesh size is enlarged in this figure, to ensure great visibility. However, before the simulation procedure, a mesh independence study was carried out, which can be found in the Appendix B.1. The pressure inside the cavity is defined as a *gauge* pressure. The models were meshed accordingly to the geometry, however one could think that for the shell, we could've used shell elements to represent the geometry. This is, in fact, true, but the shell under my investigation are not thin, they are called semi-thick shells, which can be modelled favourably with 2D elements according to the literature.

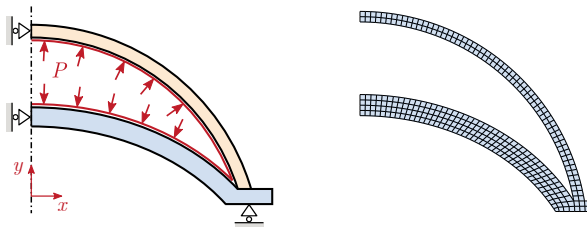


Figure 3.3: Finite element model (left) and the created mesh (right)

To fully define the problem, we also need to define the properties of the stored (or supplied) fluid. In my case, this was water, which can be modelled as an incompressible fluid in this application. Thanks to the *Fluid Cavity interaction*, the system's pressure-volume curve can be instantly obtained after solving the model.

3.2.2 Automatic simulation environment

After I found the optimal settings to create a simulation model, I created a program code, which is automatically capable of simulating models with several combination of geometric parameters. The input parameters can be specified by the user as a vector, which encapsulates the range to be calculated by the software. This process' block diagram can be seen on Fig. 3.5 below. As we can see, the software is based on scripting ABAQUS using the open-source PYTHON programming language. The output form the model is

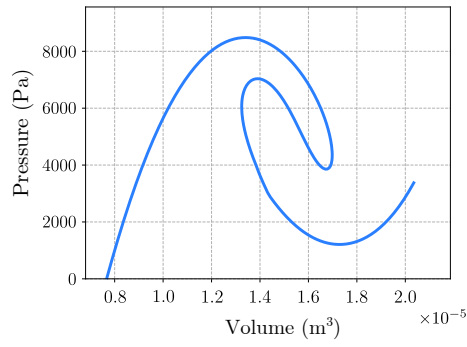


Figure 3.4: The obtained equilibrium path

the characteristic curve of the inner shell. It is important to note, that from this pressure-volume curve the energy release during the instability can also be calculated (however this property will not be widely used in this paper).

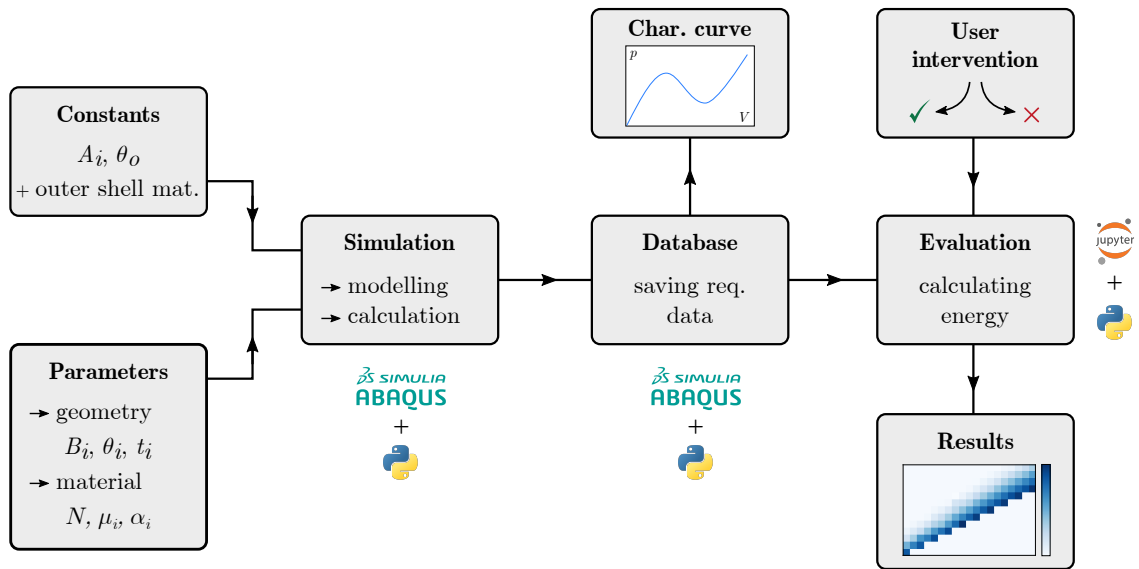


Figure 3.5: Block diagram of the simulation environment

4

Experimental testing

The goal of this chapter is to introduce the experimental setup which was developed and built to carry out measurements. In the literature we can find multiple solutions to measure the snap-through phenomena, because it has not been established which one is the best (probably we can't even highlight one as the best because of the wide variety of designs and geometries), there are still a lot of open questions. For example, there exist methods which are based on the inflation of a cavity [17, 20], but others used force measurements to capture a characteristic curve of the system [21, 22], or an image processing to determine the area of the buckled region [23].

4.1 Overview of the test setup

4.1.1 The fluidic control board

As we previously discussed in *Chapter 3* the finite element models are constructed in such a way, that the snapping behaviour of the inner shell is induced by the inflation of a fluid cavity. This is the main idea of my measurement setup as well [3, 17].

For this purpose, we have to supply the fluid with enough pressure, which can be done by using a *diaphragm pump*. The fluid flow in the system needs to be controlled, because after inflation, we have to deflate the setup, so we need some control elements as well, which can be chosen as *solenoid valves*. These valves can be operated by analog electric signals to open and close the routes of the fluid. Probably the most important part of the measurement setup is the *pressure sensor* which captures the instantaneous

gauge pressure in the system at each measurement point we define. To obtain the characteristic (pressure-volume) curve of a shell, we also have to monitor the fluid flow rate (to express the volume change), which is deduced from the voltage of the pump, because it shows nearly linear characteristic (for more information, see [Appendix C](#)). We also have to create some kind of measurement container, which is capable of hermetically sealing the shell from the environment, and capable of withstanding the pressures (which are very low in general, so the structural integrity will not cause any problems). After all, we need an *electric circuit* with a *controller*, which is capable of connecting and controlling these parts that make up the setup. To enable the data acquisition and control, we have to connect our microcontroller to a computer, where we can define the input values, and capture the output values of the sensor. Based on these ideas, a basic sketch of the setup can be seen on [Fig. 4.1](#) below.

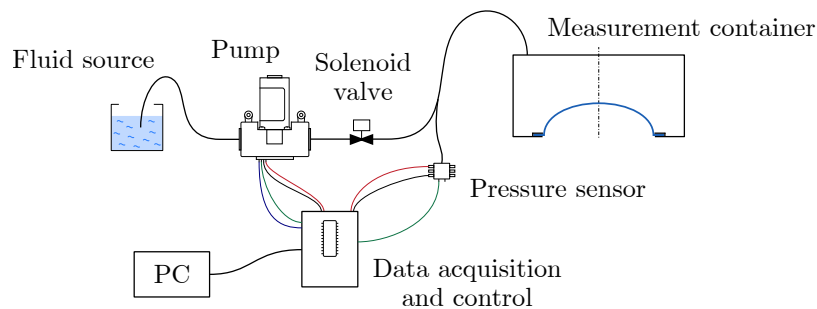


Figure 4.1: The main skeleton of the test setup

The **diaphragm pump** was chosen to be the *Kamoer KLP01* diaphragm pump, which is capable of providing 3 bar pressure with 400 ml/min flow rate, and it can operate with non-corrosive liquids, such as water. These properties are more than enough if we take into account the scale of the measurements. It can be controlled by a single voltage input (with a nominal value of 12 V, but it was found out that it can operate above 5 V).

Two **solenoid valves** were introduced into the test setup, due to the necessity of the flow control. These solenoid valves were chosen from the *M&M* company, with a model number of *D263DVG* with the corresponding coil *7250*. Their supply voltage is 24 V, and they can be operated using PWM signals provided by a *MOSFET*, which is very advantageous of the electrical control. One of the solenoid valve opens the route, so the pump can inflate the cavity, while the other opens another route, which is used to release the pressure (and the fluid) from the container.

To supply these components, we need to create 12 V and 24 V signals, which can be done by the two **DC-DC converters**. As their name suggests, they can convert a DC signal obtained from the laboratory power supply to the desired values.

The **pressure sensor** was chosen according to the specific pressure ranges. The selected model was the *Betterbeita BT-P8000* with a measurement range of 0-30 kPa and with a measurement accuracy of 0.01 kPa on the full scale. It is capable of withstanding gases, and non-corrosive fluids as well. It has a G1/4" connection, which determined

that the whole system of hydraulic components should have this connection, to ensure easy integration.

The **control** of the board and the **data acquisition** was done by an **Arduino UNO R3**, which has limited capability's compared to other microcontrollers, but this drawback is balanced by its simplicity and ease of use. This microcontroller and it's interface was used to program the software which is capable of controlling the board with two different methods, which is explained in detail at [Section 4.2](#). The most important part of the electrical subsystem of the board is that we have to open and close the solenoid valves with respect to the desired output of the system, which can be done by implementing a *PID controller*. The solenoid valves are controlled by **MOSFETs**, which has the exact type of *FR120N-M*.

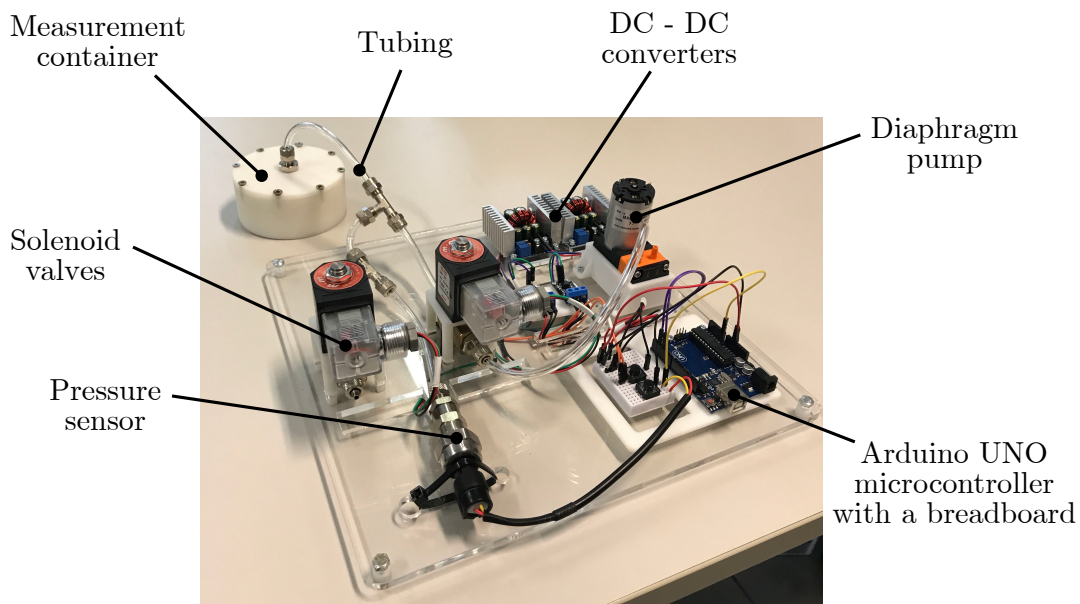


Figure 4.2: The fluidic control board with all subsystems

4.1.2 The measurement container

The measurement container is a 3D printed container which is capable of securing the shell in place. The geometry is constructed in such a way that it is easy to print it out, and it is self sealing without any additional components added. Notice, that we enhance the silicone shell to create a sealing, so no fluid is lost during inflating the cavity. The top hole is the position of the connector element, which is used to connect the measurement container to the fluidic control board. Notice the bottom hole, which is large enough to ensure the free snap-through motion of the shell. The CAD model of the container can be seen on [Fig. 4.3](#) below.

It is very important to note, that the shape of the measurement container differs from the shape of the outer shell on [Fig. 3.1](#). This is due to the simplification of the geometry: this cylindrical geometry is very simple to print out with great accuracy, conversely to the introduced outer shell in the finite element model. As a consequence of this, the

volume of the cavity won't match for a specific shell between the measurement setup and the numerical calculation. However this is not a problem, because instead of the volume as a parameter for evaluating the results, we can use the change of the volume, which will be the same regardless of the shape and size of the cavity. This simplification can be made, because the pressures are so low in the system that they will not deform the ABS container during the measurement significantly. To prove this, I made a simple finite element analysis, which can be seen at [Appendix B.2](#). This mapping between the actual volume and the volume change can be done by shifting the volume axis with the initial volume for both the numerical and the test results as well.

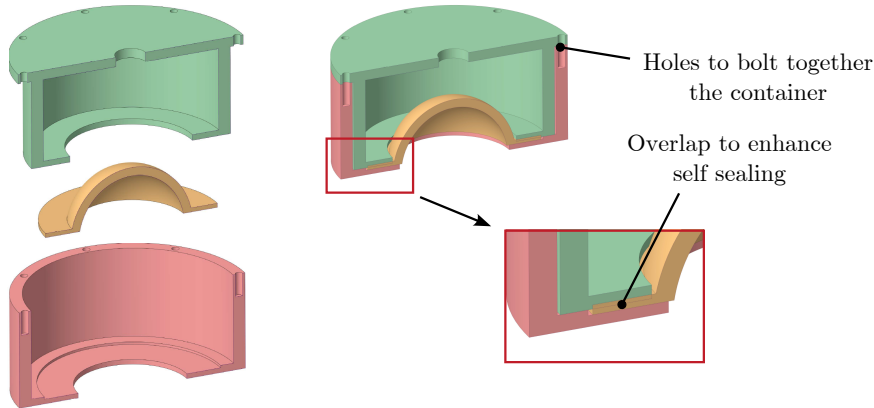


Figure 4.3: The CAD model of the measurement container showcasing the sealing solution

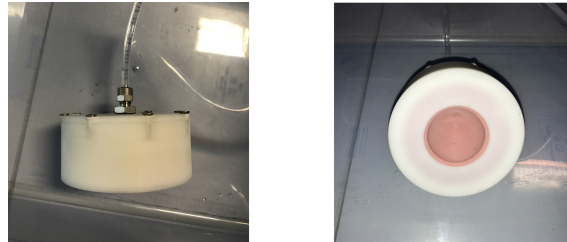


Figure 4.4: The final 3D printed measurement container with a shell placed inside

4.1.3 Specimen fabrication

The shells were fabricated out of the two component silicone *ELASTOSTIL M 4061*. It is a pourable, addition-curing silicone rubber, which vulcanizes at room temperature. Based on the manufacturer it is perfect to create shrink-free molds [24].

Property	Component A	Component B
Color	White	Reddish brown
Density at 23 °C	1.14 g/cm ³	1.01 g/cm ³
Dynamic viscosity	15000 mPa · s	800 mPa · s

Table 4.1: The properties of the components

The two component need to be mixed in a ratio of 9:1 (A:B), which were done in paper cups using a precision scale.

Two comonent poured together



Two component after stirring



Figure 4.5: The two component in the mixing phase

After mixing, the silicone was placed inside a vacuum chamber, which is responsible for removing air bubbles from the material before curing. This step ensured, that the silicone material is homogeneous and specimens are high quality shells.



Figure 4.6: Degassing the silicone in the vaccuum chamber

After this, the silicone is poured into 3D printed molds, according to the required geometry. The CAD model and its features can be seen on Fig. 4.7 below.

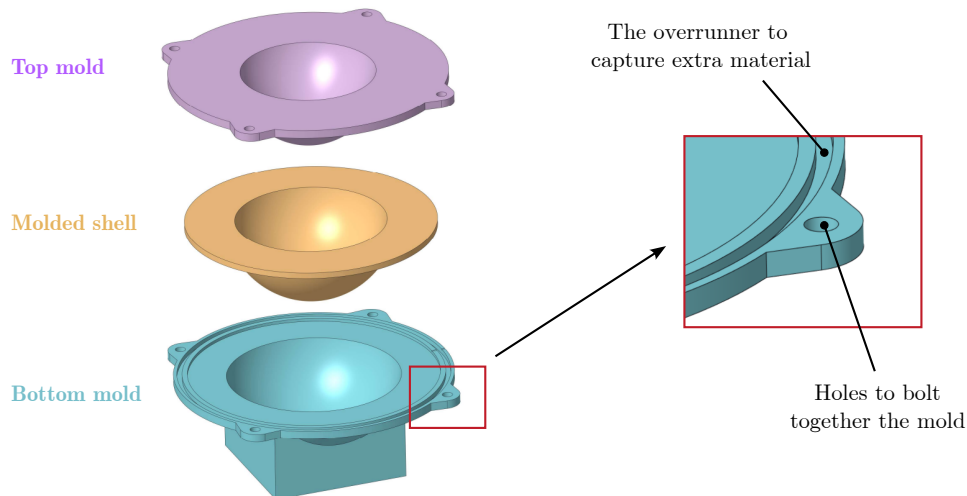


Figure 4.7: The CAD model of the mold

The geometric model of the mold is also parametric, so it changes its shape according to the desired shell geometric parameters. The molds were 3D printed on a *Zortrax M200 Plus* printer, with ABS filament.

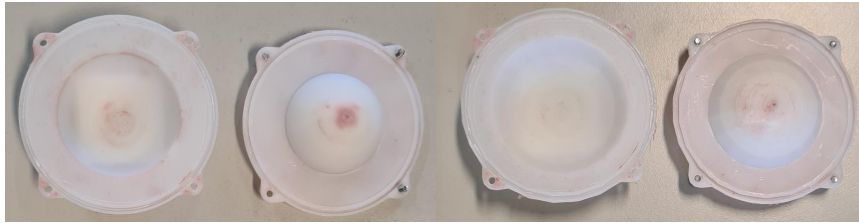


Figure 4.8: Different sizes of 3D printed molds

After the silicone was poured inside the forming cavity of the molds, the two halves were locked together with bolts to ensure that the shell doesn't push the mold apart. The silicone will eventually cure in room temperature as well, but it would need at least 12, but favourably 24 hours. To speed up this process, I placed the mold into a drying chamber, which was set to 65°C, which is high enough that the silicone will cure in about 20 minutes, but not as high that the ABS material of the mold will not deform due to the resultant thermal stress.



Figure 4.9: The curing process in the drying chamber

The shells can be easily removed from the molds, and if needed the external material can be cut off from the overrunner part. One of the fabricated shell can be seen on Fig. 4.10 below.



Figure 4.10: The final silicone shell

4.1.4 Determination of the material parameters

As in all numerical calculations, simulations require the material parameters for the corresponding material model, which is used to describe the response of the material.

As it was proposed in Section 2.1.4, the Ogden hyperelastic model was used to capture the silicone's behaviour. To be exact, I used to use the second order Ogden hyperelastic model (multiple models were tested, and found this one as the most accurate), which is defined by 4 material parameters μ_1, μ_2, α_1 and α_2 , which were determined by uniaxial tensile and compression test using the *Instron 3345 Single Column Universal Testing System*, equipped with and *Instron 2519-107 5 kN load cell*. First, tensile test were performed on bone-shaped (ISO 37 standard) specimens with different thicknesses, to capture the transversal stretch component of the material. The transversal and longitudinal stretch component were find by *image processing (binarization)*, and it was found that the used material is incompressible, where the stretches (for the uniaxial test case) can be written as:

- in the direction of tension: λ_1 ,
- in the transversal direction: $\lambda_2 = \lambda_3 = 1/\sqrt{\lambda_1}$,

which satisfies the expression $J = \lambda_1 \lambda_2 \lambda_3 = 1$, for incompressible materials.

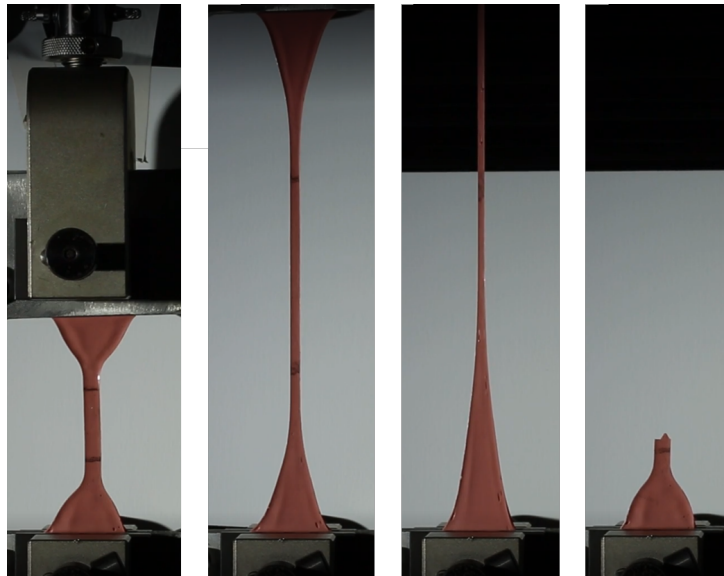


Figure 4.11: Bone-shaped specimens during tensile testing according to *ASTM D395-03*

After this, compression tests were performed on two cylindrical specimens (with two different diameters), which is equivalent to equibiaxial tension tests, through the superposition of hydrostatic stress. It states that if a fully incompressible material is subjected to uniaxial tension (uniaxial compression), it's equivalent to an equibiaxial compression (equibiaxial tension).

The compression tests performed on the cylindrical specimens with the *binarization* as a result processing method can be seen on Fig. 4.13.

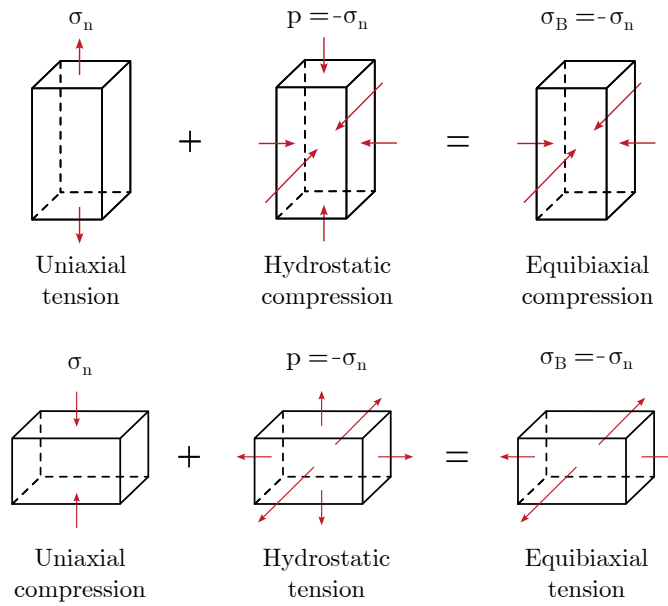


Figure 4.12: Equivalent experimental test for fully incompressible materials

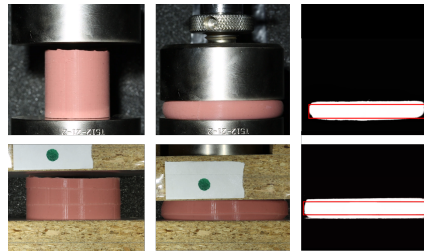


Figure 4.13: Compression test on cylindrical specimens

These tests resulted into several force-displacement (which has been converted into nominal stress-stretch) curves, which represent uniaxial and equibiaxial tests. We can use the closed form solutions of the second order Ogden hyperelastic model in these stress states to fit the model parameters. The solution for the nominal stress in the uniaxial case can be written as [7]:

$$P = \sum_{k=1}^2 \frac{2\mu_k}{\alpha_k} \left[\lambda^{\alpha_k - 1} - \lambda^{-\alpha_k/2 - 1} \right]. \quad (4.1)$$

Defining the error-function as the root means square error as

$$\text{RMSE} = \sqrt{\frac{1}{M} \sum_{i=1}^M \left(\frac{P_i^{\text{mod}} - P_i^{\text{exp}}}{P_i^{\text{exp}}} \right)^2}, \quad (4.2)$$

where M are the number of the datapoints, P_i^{mod} is the nominal stress given by the model (by the stretch and the intermediate model parameters as the input) and P_i^{exp} denotes the experimental value of the nominal stress. By utilizing the *optimize* function of the SCIPY module found in the PYTHON programming language, we can easily obtain the model parameters corresponding to the measurement data, with the above give error function. The fitted model and the parameters can be seen on the figure below.

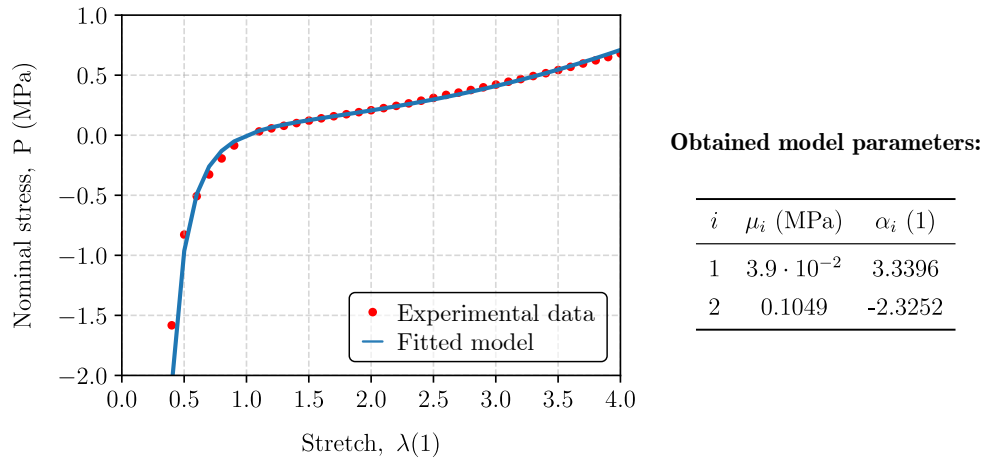


Figure 4.14: The fitted second order Ogden model and the obtained model parameters

4.2 Controlling the measurement board

4.2.1 Volume and pressure control

As it was previously discussed in [Section 2.2](#), the nonlinear system can be solved with force (which is the pressure in this case) or displacement (which is the volume change) control. This two method opens the two possible control method for the measurements as well:

1. Volume control method,
2. Pressure control method.

From these, the **volume control** is a simpler method, because the volume change can be explicitly controlled by the pump via the known characteristic of the pump which was described in [Appendix C](#). We know the volume flow rate for every input voltage on the pump, so we can create several input profiles which defines the change of the cavity volume.

The **pressure control** method is the harder method, because we can only control the pressure in the system through setting different volume flow rates. To be able to control the pressure, we would need to derive the relationship between the pressure and the volume. Once this relationship is known, a controller can be designed and its parameters could be derived. Unfortunately, these governing equations (to the best of the author's knowledge) has been not derived yet for this exact problem (considering moderately thick shells, with incompressible hyperelastic materials). To overcome this difficulty, we can implement a simple *PID controller* and define its parameters from measurements, which we are able to do by utilizing the volume control method. The essence of this control method can be found in the next section.

4.2.2 The PID controller

Nowadays the *Proportional–Integral–Derivative* (*PID*) controller is one of the most widely used type of the closed-loop control methods. The goal of the controller is to produce a control signal that can dynamically minimize the difference between the current output and the desired output of the system.

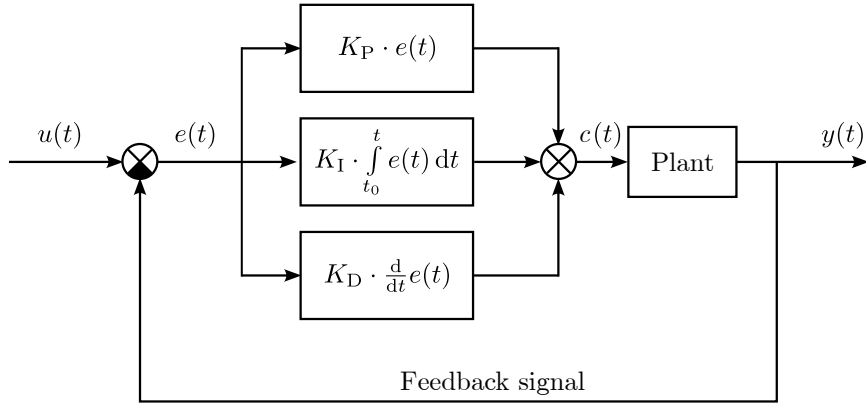


Figure 4.15: The schematic diagram of the PID controller

The essence is that we create a negative feedback in the system, which is used to create the so-called error signal $e(t)$. The controller interprets this signal, and calculates how to manipulate the control signal $c(t)$ of the plant to reduce the error between the input $u(t)$ and the output $y(t)$. The controller can be tuned with the help of the three constant parameters K_P , K_I and K_D . The controller manipulates the control signal with respect to „history” (integral), the „present” (proportional) and the „future” (derivative) value of the error signal. The values of these three parameters defines how fast the controller works, what is the overshoot value, how fast it stabilizes the output, etc. This paper is not addressed for a complete description of the *PID controller*, however these parameters needs to be defined, which can be done by analysing the governing equations. But nowadays, engineers often use several tools to obtain numerical values which can be tested, and iterated until they are sufficient for the controller which is designed for that specific problem. This is the method that I followed as well: the MATLAB software has very handy tools to identify your system based on measurement data, and tune a *PID controller* for it. As we said previously, with the volume control method, we can already create a measurement, which has an input signal defined by the Heaviside step function as

$$H(x) = \begin{cases} 1, & x \geq 0, \\ 0, & x \leq 0. \end{cases} \quad (4.3)$$

The input signal in this case is the voltage of the pump, so using t for the time:

$$U(t) = \begin{cases} 12, & t \geq 0, \\ 0, & t \leq 0, \end{cases} \quad (4.4)$$

which essentially means that the pump was turned on with 12 V of voltage at the time $t = 0$ and it stayed on this constant value during the whole measurement. Meanwhile the pump is inflating the cavity, we can log the corresponding pressure data from the transducer. The acquired pressure-volume change curve can be seen on Fig. 4.16 for the shell with $A_i = 22$ mm, $B_i = 22$ mm, $t_i = 3.5$ mm and $\theta_i = 65^\circ$, with a constant 12 V of input voltage. Utilizing the *PID tuner* app from MATLAB, we can import this output signal, and specify that this is our system's response for the input described in Eq. (4.4). After this, the software will identify a plant. Of course, the identification will not be a 100% accurate, but this method is still far better to estimate the control parameters instead of just trying a bunch of combinations.

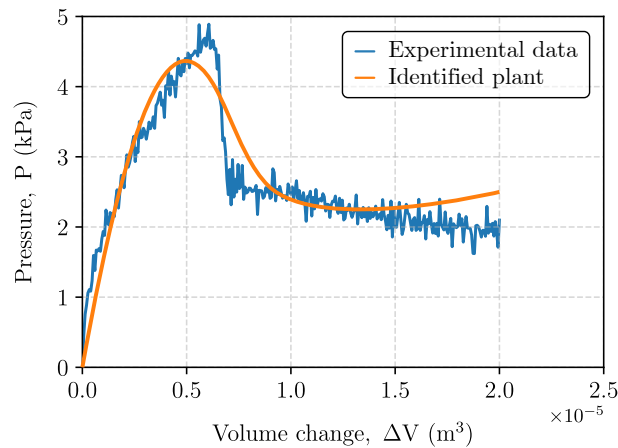


Figure 4.16: An experimental result with the volume control method, and the identified plant based on it

My goal during the tuning of the controller was to shorten the raise time as much as possible while keeping the overshoot value as low as possible. The graphical user interface helps us to see how the response of our system changes with the modification of each parameters. MATLAB has a function to automatically define the parameters which results in a stable system. I used this option to initialize the parameters of the controller, but after that I tuned them myself to get a slightly better response.

Parameter	Value
K_P	132.2
K_I	226.6
K_D	15.1

Table 4.2: The obtained *PID controller* parameters

The graphical user interface of the software can be seen below on Fig. 4.17. At the controller section, we can choose what type of controller we want to tune (P , PD , etc.) which was PID in my case. The controller tuning menu bar provides tools to tune the parameters of the selected controller, while the options on the right side of the screen are corresponds to saving and exporting the tuned plant and controller parameters.

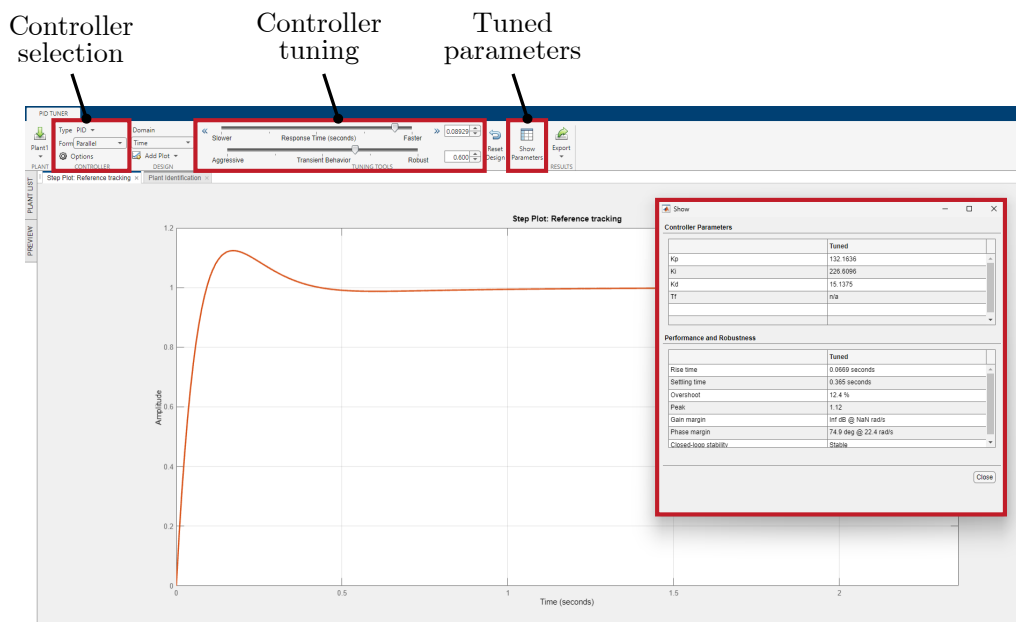


Figure 4.17: User interface of the *PID tuner*

4.3 Measurement test procedure

The list below conducts the tasks we need to perform to successfully repeat a test:

1. Place the shell inside the measurement container, and tighten the container with the bolts.
2. Connect the hydraulic tubing of the system to the measurement container.
3. Connect the PC to the microcontroller.
4. Ensure, that the volume of the supplied fluid is enough to inflate the cavity.
5. Prepare an empty vessel for the overflow branch of the hydraulic system.
6. Select a preferred control method, and set the desired value of the output value.
7. Check if there are no visible shorts in the circuit and no visible damage on the hydraulic / electronic components.
8. Connect the DC-DC converter to the power supply.
9. Turn on the test setup, and start inflating the hydraulic system, to ensure that no air is left in the closed system.
10. Start the measurement by the dedicated buttons on the breadboard.
11. Log the measurement data (for example *Microsoft Excel* can be used for this).

5

Analytical modelling

The goal of this chapter is to present the analytical modelling of the critical pressure, which initiates the snap-through behavior.

5.1 Shell theory for circular shells

Let us consider an element $OABC$ cut out from a spherical shell (defined by radius a) by two meridional section an angle $d\psi$ apart and by two conical surfaces normal to the meridians and inclined to the axis of symmetry by the angles θ and $\theta + d\theta$. Introduce a coordinate system at O , with the x and y axis being tangent to the surface, while axis z point in the radial direction. The infinitesimal deformation at point O in the directions defined by the coordinate system is denoted by u, v and w respectively. If we are considering symmetrical deformations, only u and w differs from zero [25].

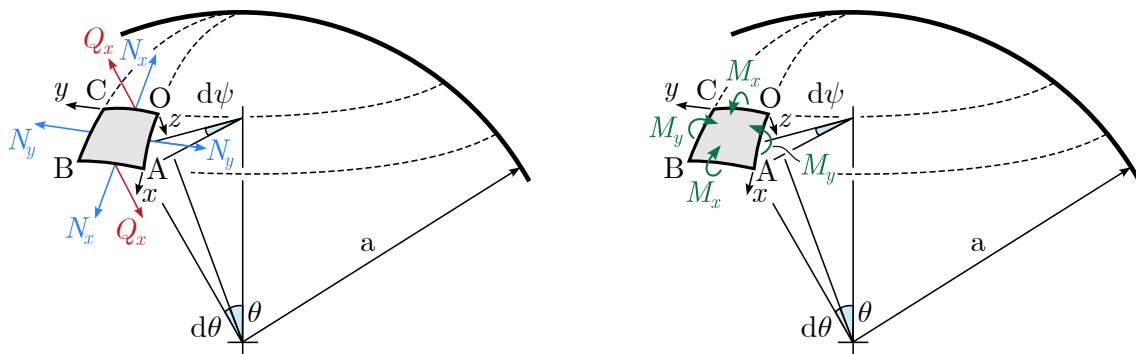


Figure 5.1: The forces and moments acting on a shell element, redrawn from [25]

The forces acting on the element can be seen on Fig. 5.1 below, where is important to note, that the forces and the moments act simultaneously, however they are displayed on different figures to enable great visibility of all components. With these considerations, we can define the equilibrium state of the shell element with three equations: projections of all forces on the x and z axis and the moments of all forces with respect to the y axis. By assuming that the external loading (if there is any) is normal to the shell's surface, the equilibrium equations can be written as [4, 25]:

$$\begin{aligned} \frac{dN_x}{d\theta} + (N_x - N_y) \cot(\theta) - Q_x + N_y \left(\frac{u}{a} + \frac{dw}{a d\theta} \right) - Q_x \left(\frac{d^2w}{a d\theta^2} + \frac{w}{a} \right) &= 0, \\ \frac{dQ_x}{d\theta} + Q_x \cot(\theta) + N_x + N_y + qa + N_x \left(\frac{d^2w}{a d\theta^2} + \frac{dw}{a d\theta} \right) + N_x \left(\frac{u}{a} + \frac{dw}{a d\theta} \right) \cot(\theta) &= 0, \\ \frac{dM_x}{d\theta} + (M_x - M_y) \cot(\theta) - Q_x a + M_y \left(\frac{u}{a} + \frac{dw}{a d\theta} \right) &= 0, \end{aligned} \quad (5.1 - 5.3)$$

where the forces can be written as

$$N_x = -\frac{qa}{2} + N'_x \quad \text{and} \quad N_y = -\frac{qa}{2} + N'_y \quad (5.4)$$

where N'_x and N'_y are the resultant forces due to the displacements u, v and w , while q is the intensity of the distributed load. We can use Eq. (5.1) and Eq. (5.2) to eliminate Q_x , we can obtain the resultant forces, which can be substituted back to Eq. (5.3) leading to a partial differential equation system for u and w as

$$M_x = -\frac{D}{a^2} \left[\frac{du}{d\theta} + \frac{d^2w}{d\theta^2} + \nu \left(u + \frac{dw}{d\theta} \right) \cot(\theta) \right], \quad (5.5)$$

$$M_y = -\frac{D}{a^2} \left[\left(u + \frac{dw}{d\theta} \right) \cot(\theta) + \nu \left(\frac{du}{d\theta} + \frac{d^2w}{d\theta^2} \right) \right], \quad (5.6)$$

where D is a constant (known as flexural rigidity) obtained from geometric and material parameters [25]:

$$D = \frac{Eh^3}{12(1-\nu^2)}, \quad (5.7)$$

where E is the Young's modulus, h is the thickness of the shell and ν is the Poisson ratio.

The solution methodology of these two equations is not presented in this paper, due to its length, but it can be found in the literature [4, 26, 25]. Zoelly was the first, who obtained the formula for the critical (smallest) pressure for spherical shells at which buckling may occur:

$$q_{cr} = \frac{2E}{\sqrt{3(1-\nu^2)}} \left(\frac{h}{a} \right)^2 \quad (5.8)$$

It is interesting to note, that this buckling type of spherical and cylindrical shells were studied intensively in the 20th century. However most of these studies were performed on very thin shells, which has a ratio of $h/a \ll 1$ [26, 27, 28, 29]. The theory was not defined for thick shells until *Hill* proposed a new method, where the calculation of this critical pressure involves solving a fourth-order system of highly non-homogeneous differential equations [30, 31]. Note, that *Hill* proposed this method for two type of hyperelastic materials, however the solution is dependent on the strain energy function of the material [30], which has been not yet developed for my choice of material model.

It is also remarkable, that a systematic discrepancy was found between the theoretically calculated and experimentally obtained values. The theoretical values in some cases were 3 to 4 times higher than what the experiments predicted. First the boundary conditions were analysed, after several attempts were made to lower the theoretical values by taking into account the initial imperfection of the spherical shell [26].

5.2 Proposed method for elliptical shells

The introduction of the theory above are valid only for spherical shells. The same theory cannot be applied for my elliptical shell, because of the geometric difference, however, an estimation could be done to find the *equivalent circle* with parameters R as a radius and θ_{ic} as the opening angle, which has the closes circular segment compared to the elliptical segment defined by the two semi-axes A_i, B_i and by the opening angle θ_i .

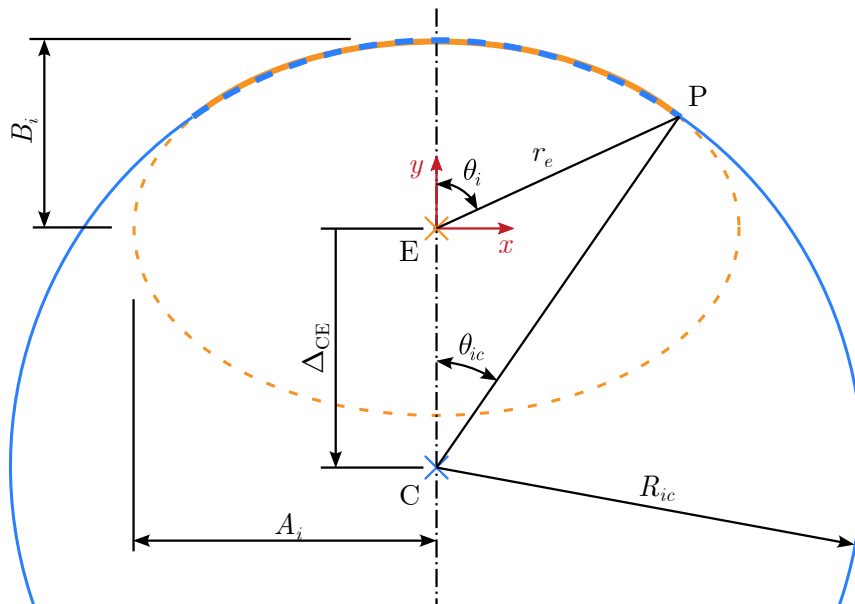


Figure 5.2: The elliptical segment (orange) and a very good approximation by a circular segment (dashed blue)

Introduce a simple drawing of the shells' mid planes, to be able to establish the relationship. The curvature is a measure of curve at an arbitrary point, that defines how much the curve is deviated from a straight line.

Mathematically, it's expressed as

$$\kappa = \frac{1}{R_{\text{osc}}}, \quad (5.9)$$

where R_{osc} is the radius of the osculating circle. We can notice, that if $B_i < A_i$, then the elliptical segment has smaller curvature, thus the radius of the equivalent circular segment has to be bigger than A_i . As a consequence of this, the circle's centerpoint has to be shifted down with a quantity denoted by Δ_{EC} (note that Δ_{EC} defined as the distance from point C to point E , which is a negative value). Conversely, if $B_i > A_i$ then the radius of the circle R has to be smaller than B_i and the circle is shifted upwards, which results in a positive value of Δ_{EC} . Of course, in the trivial case when $A_i = B_i$ then the elliptical segment degenerates to a circular segment, so in this case we don't have to make any calculations.

By taking the ECP triangle, we can notice that from the parameters R, R_e and θ_i we can calculate the opening angle of the equivalent circle by the law of sines as

$$\theta_{ic} = \arcsin\left(\frac{r_e}{R} \sin(\pi - \theta_i)\right), \quad (5.10)$$

where r_e is the length of the line drawn from the elliptical segment's origin to an arbitrary point of the ellipse defined by θ_i , according to Fig. A.2.

This opens the route, to write an optimization script, which takes in the parameters of the elliptical segment (A_i, B_i, θ_i) and finds the parameters of the equivalent circular segment (R, θ_{ic}). The script was written in PYTHON and it follows these steps:

1. Taking the input of the elliptical segment.
2. Calculating the points of the elliptical segment.
3. Defines a function, which calculates the corresponding y coordinates a circular segment for given x coordinates.
4. Utilizing this function, and the known x and y coordinates of the elliptical segment, the script iterates the value of R_{ic} and Δ_{EC} until convergence reached based on an initial guess, which can be made as explained above.
5. The output of this optimization is R_{ic} and Δ_{EC} , from which the opening angle θ_{ic} is calculated.

The written script can be seen in [Appendix D](#).

From now on, the Eq. (5.8) can be used to estimate the critical pressure of the elliptical shells, using this conversion for the radius.

6

Comparison and conclusion

6.1 Comparison of the presented methods

The comparison starts by defining the geometric parameters of the shells which were used to test the presented methods. Three types of shells were used, which were only different in the parameter B_i . These values were determined with a preliminary study using the the automatic simulation environment. The simulation predicted that these shells will behave ideally which enables us to do a qualitative and quantitative comparison between the methods. Notice that one of the three shell are spherical, where $A_i = B_i$. The material model and its parameters were the same for every model, which were discussed [Section 4.1.4](#).

No.	A_i (mm)	B_i (mm)	t_i (mm)	θ_i (°)
1.	22	18	3.5	65
2.	22	22	3.5	65
3.	22	26	3.5	65

Table 6.1: The geometric parameters of the specimens

6.1.1 Results of the simulations

First, the results of the finite element simulation were evaluated, which resulted in the graph which can be seen on [Fig. 6.1](#) below. The darkness of the line represent the higher

values of B_i according to the legend on the right of the figure. We can see that the snap-through phenomena is present in all three of the curves, however the snap-back effect is only present on the shells with bigger semi-minor axis. This is happening because more material needs to be fit through the same space, because A_i is fixed, thus the width of the shells are equal, while their height differs with 20% and 40%.

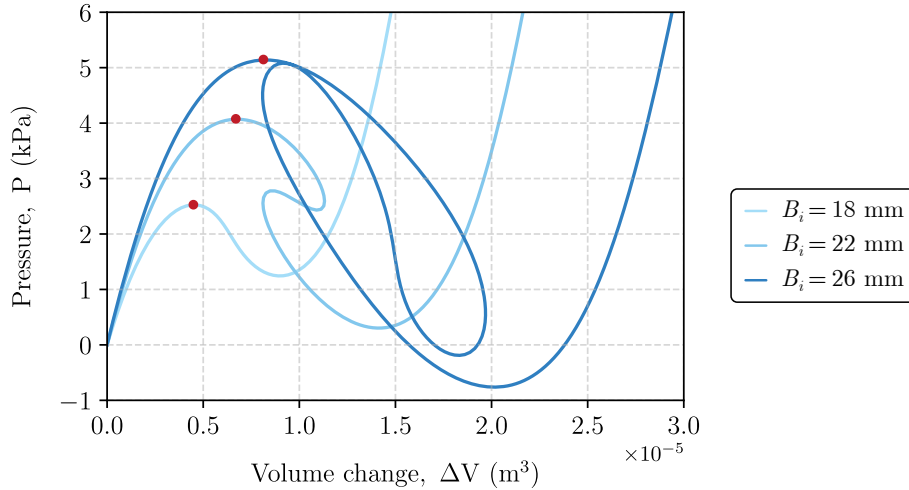


Figure 6.1: The characteristic curves of the shells acquired by simulation

The critical pressures are located at the local maxima of the curves, before the snap-through, which is denoted by a red mark on the figure. Table 6.2 summarizes these obtained critical values.

No.	B_i (mm)	P_{cr}^s (kPa)
1.	18	2.525
2.	22	4.069
3.	26	5.139

Table 6.2: The obtained values for the critical pressure based on the simulations

6.1.2 Results of the measurements

During the experimental testing, I followed the proposed test procedure described at Section 4.3. The sampling frequency of the data was 500 Hz for every measurement. The measurement container were inflated with water. I performed three measurement for every shell, and for every method, thus in total $3 \cdot 3 \cdot 2 = 18$ measurement were carried out. The data acquisition was performed via the USB connection between the PC and the *Arduino UNO R3*, and the measurement files were saved as comma-separated values.

Volume controlled case

Regarding the volume controlled case, the inflation was performed with a constant volume flow rate, which was 400 ml/min, which represent the 12 V input voltage on the pump. The figure below showcases the acquired data from the three measurement per shell as a point cloud (pale red color). The averaged values of the measurement data can be seen with a continuous red line, while the simulation data for comparison is plotted with a pale blue.

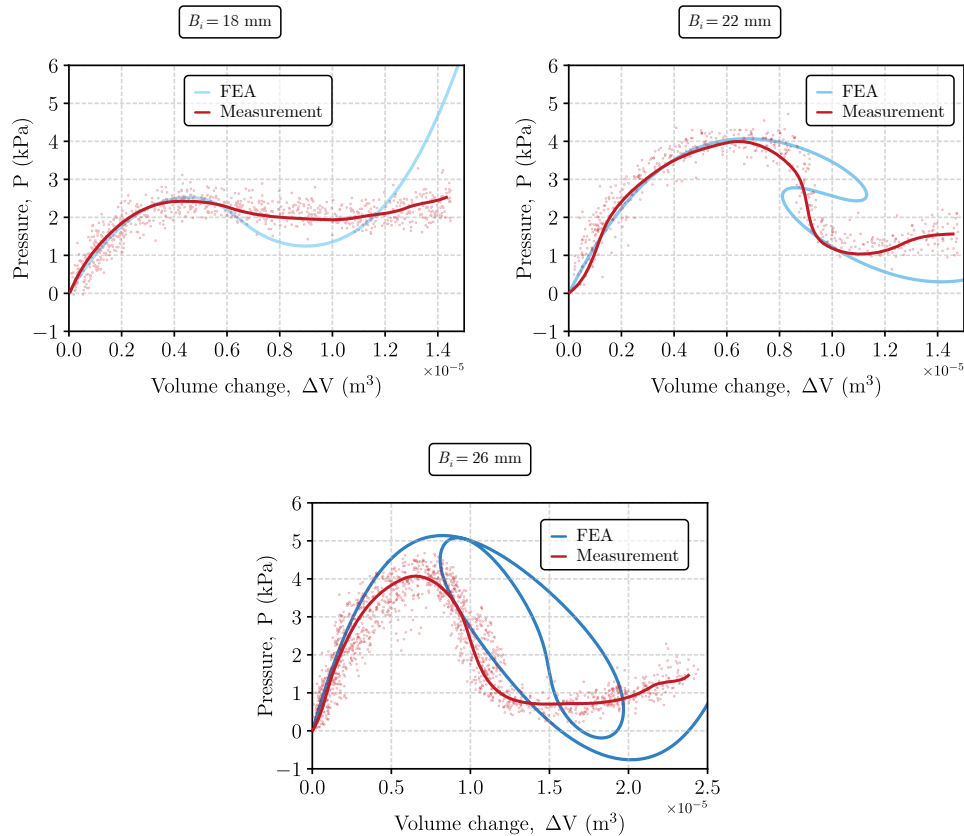


Figure 6.2: The results of the measurements when using the volume controlled method

As we can see, the measurements were following the equilibrium path of the system quite well at the start of inflation procedure. The smaller shells were approximately reached the critical pressure which were predicted by the simulations, but the third specimen with the largest semi-minor axis snapped before reaching this critical point. We can also notice that the snapping behaviour is not perfect in the measurement, because based on iterative procedures, we should see only a vertical line when the snapping happens, like the theory of the solution of nonlinear system describes (see [Section 2.2](#)). This could happen due to a lot of reasons, we could mention the imperfection form of the fabricated shell, or the discrepancy of the pump, which is not a precision measurement device, the volume flow rate can differ a bit due to the increasing pressure in the system. The critical pressures were defined as the local maxima of the actual measurement curve, independent of where the simulation predicted it previously. The biggest differences obviously emerged at the shell with $B_i = 26$ mm, which could've been expected, because this shell's behaviour is

the stiffest, thus the symmetric conditions will surely break in all test cases. The obtained values based on the measurement data can be summarized in the following table:

No.	B_i (mm)	P_{cr}^{mv} (kPa)
1.	18	2.375
2.	22	3.921
3.	26	4.078

Table 6.3: The obtained values for the critical pressure based on the volume controlled measurements

Pressure controlled method

The pressure control method is more advanced than the volume control method, it involves the usage of the *PID controller*. The desired pressure value was determined using the previous simulations and the volume controlled measurements. This was in every case 120% of the lowest predicted critical pressure, to initialize the snap-through. The results of the measurement compared to the simulation can be seen on the graphs below.

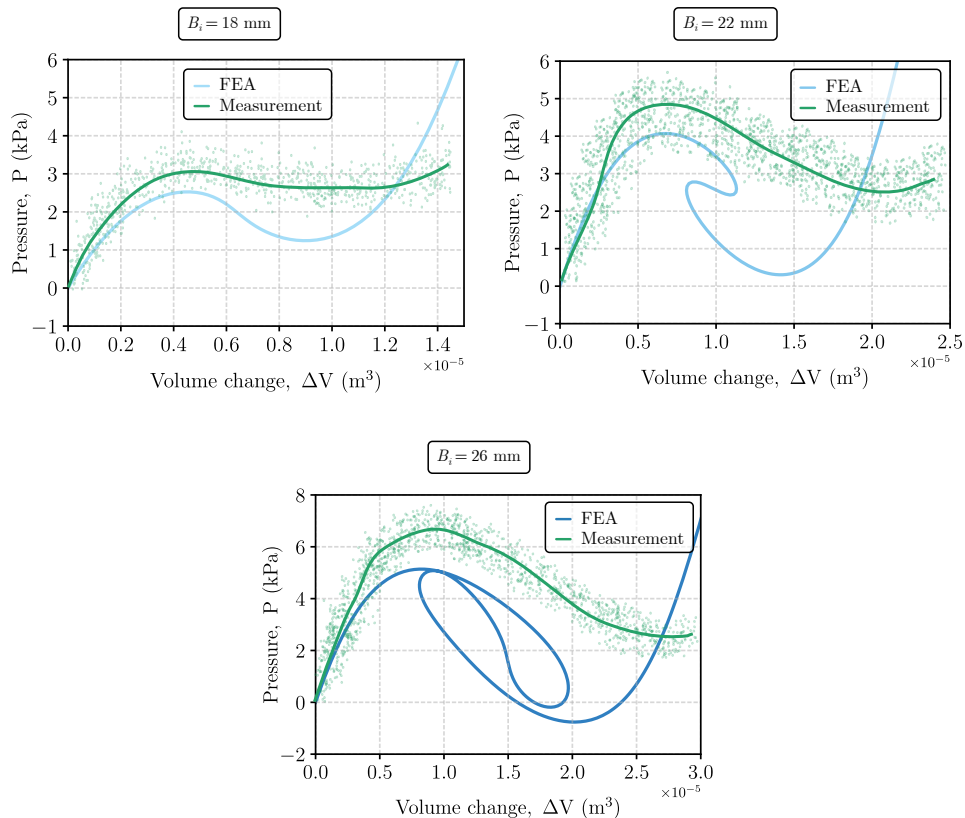


Figure 6.3: The results of the measurements when using the pressure controlled method

We can see that the measurements overshoots the predicted equilibrium curve for each shell. This is probably due to the imperfections introduced in the measurement setup.

We also can't recognize clearly the snap-through phenomena what the theory states (we should jump on a vertical line, according to the force controlling method described in [Section 2.2](#)). This is probably due to the small pump, because when the shell snaps, we can't produce the required pressure that quickly. This can be solved by implementing a buffer container, which is pre-pressurized by a stronger pump, and we control the system from this passive pressure source. The critical pressures can be stated as follows:

No.	B_i (mm)	P_{cr}^{mp} (kPa)
1.	18	3.087
2.	22	4.832
3.	26	6.786

Table 6.4: The obtained values for the critical pressure based on the pressure controlled measurements

However we are not experiencing the perfect behaviour, there is definitely a difference between the two different measurement method: the volume control method tends to follow the snap-back behavior, while the pressure control method tends to follow the snap-through phenomena, which is the expected behaviour.

6.1.3 The analytical calculations

In order to use the analytical equation derived from the shell theory, we need to find the equivalent circle's parameters for the elliptical shells, which can be done by utilizing the method provided in [Section 5.2](#). [Table 6.5](#) summarizes the input and obtained parameters as well.

No.	A_i (mm)	B_i (mm)	t_i (mm)	θ_i (°)	R_{ic} (mm)	θ_{ic} (mm)
1.	22	18	3.5	65	24.62	50.92
2.	22	22	3.5	65	22	65
3.	22	26	3.5	65	20.60	83.42

Table 6.5: The obtained parameters for the equivalent circles

Now, we can utilize the formula from [Eq. \(5.8\)](#) as

$$P_{cr}^a = \frac{2E}{\sqrt{3(1-\nu^2)}} \left(\frac{t_i}{R_{ic}} \right)^2, \quad (6.1)$$

where $\nu = 0.5$ (due to the incompressible material property), while

$$E = 2\mu(1 + \nu) = 0.144 \text{ MPa} \quad \text{and} \quad \mu = \sum_{i=1}^2 \mu_k. \quad (6.2)$$

After the calculation, the critical pressures are summarized in the table below.

No.	B_i (mm)	P_{cr}^a (kPa)
1.	18	11.639
2.	22	14.576
3.	26	16.625

Table 6.6: The obtained values for the critical pressure based on the analytical calculation

As we can see, these value do indeed overestimate the critical buckling pressure, with the same factor of 3-5 which can be seen on the literature too [26, 17, 29]. But after this topic has been studied intensively, the usual way of proceeding with analytical calculations is that we establish some empirical formula, based on measurement. The work of *Taeprasartsit* states that the critical pressure value is only dependent on the geometric parameters for shells that are made from the same material [28]. *Howwen* also utilized this property, which states that the critical buckling pressure takes a form of

$$P_{cr}^e = C_1 \left(\frac{t_i}{R_{ic}} \right)^2 \sin(\theta_{ic})^2 + C_2, \quad (6.3)$$

where C_1 and C_2 are constants [17, 28]. Using the volume controlled measurement method's results from the first two specimens, we can calculate the constants, which turns out to be:

$$C_1 = 179538 \quad \text{and} \quad C_2 = 188.589. \quad (6.4)$$

Based on this equation, the third specimens critical pressure can be estimated as

$$P_{cr}^{e(3)} = C_1 \left(\frac{t_i}{R_{ic}^{(3)}} \right)^2 \sin(\theta_{ic}^{(3)})^2 + C_2 = 5.303 \text{ kPa}, \quad (6.5)$$

which is above what we experience in the volume controlled measurement (4.078 kPa). But taking a look back at the simulated value, it is a very good approximation of it, the relative error is

$$\varepsilon_{cr}^{e(3)} = \left| \frac{P_{cr}^{s(3)} - P_{cr}^{e(3)}}{P_{cr}^{e(3)}} \right| \cdot 100\% = 3.09\%. \quad (6.6)$$

Of course, this approximation is only valid for these material and this measurement range, interpolated (especially extrapolated) values for different parameters should be handles with care. Of course, this constant determination could be also made from a correlation between a lot of measurements, utilizing a root means square error optimization technique for example. This was not performed in this study, because of the low number of measurements.

6.2 Conclusions

During my work we've seen simulations, measurements and analytical calculations performed in order to characterize a fairly complicated system.

Regarding the simulations, they are a useful tool to predict a shell's behaviour which is subjected to external loads, however it's hard to take into account the imperfections of the geometry, and the asymmetric deformations.

The measurements proved that the finite element simulations are close to the actual buckling mode of the shell. The measurement setup provided is capable to characterize a shell by simple and fast loading conditions. Also, it was found that the setup is capable of reproducing the measurement results, the deviation of the acquired data for a specific shell did was not significant, taking into account other imperfections in the system. Qualitatively the volume method performs better: it follows the desired path better than the pressure control method, which is probably because of the controller and the weak (slow) pump. We can also state, that the volume control method provides results with less deviation in the data.

Analytical calculations can be also a great tool to get an idea of the shell's basic behaviour. The biggest advantage of the analytical calculations that they are time and cost effective, once the theory for a specific shell type is acquired in a closed or empirical formula, then based on the input parameters the investigated quantity can be easily calculated. However these theories also do not account for the asymmetric deformations and material imperfection made on the shell. As it was discussed before, the theory's predicted values are overshooting the measured and simulated values, but in case of a design process this is a conservative approach, so the shell will be able to withstand the prescribed load.

No.	B_i (mm)	P_{cr}^s (kPa)	P_{cr}^{mv} (kPa)	P_{cr}^{mp} (kPa)	P_{cr}^a (kPa)	P_{cr}^e (kPa)
1.	18	2.525	2.375	3.087	11.639	2.375
2.	22	4.069	3.921	4.832	14.576	3.921
3.	26	5.139	4.078	6.786	16.625	5.303

Table 6.7: Comparison of all obtained values for the critical pressure

As Table 6.7 shows above, the obtained values were in a good agreement with each other. Plotting these values in a bar chart results in Fig. 6.4. We can also create a chart which shows the relative error of each method corresponding to the simulations. From these figures we can clearly see, how much the analytical values are overshooting the predicted critical pressure by the other methods. This is in agreement with the literature as said before. The smallest deviation between the numerical results were obtained for the spherical case ($B_i = 22$ mm), which can be expected: during the inflation of this shell, asymmetric deformation conditions are less likely to occur.

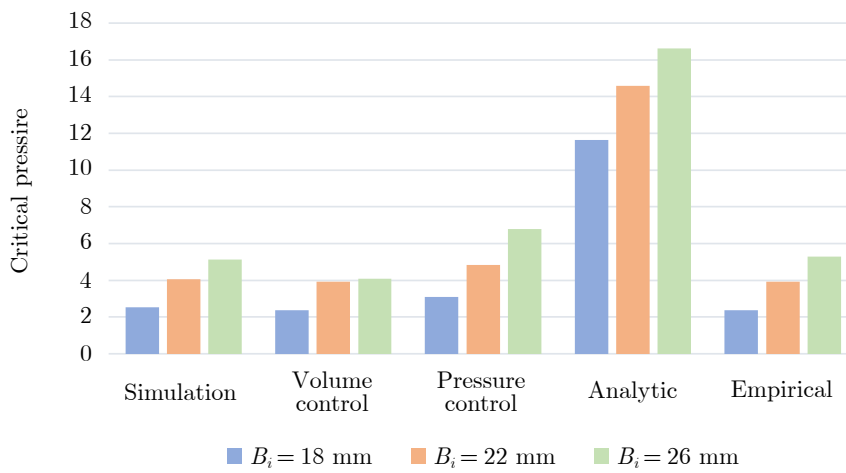


Figure 6.4: Comparison of the predicted critical pressures of different methods

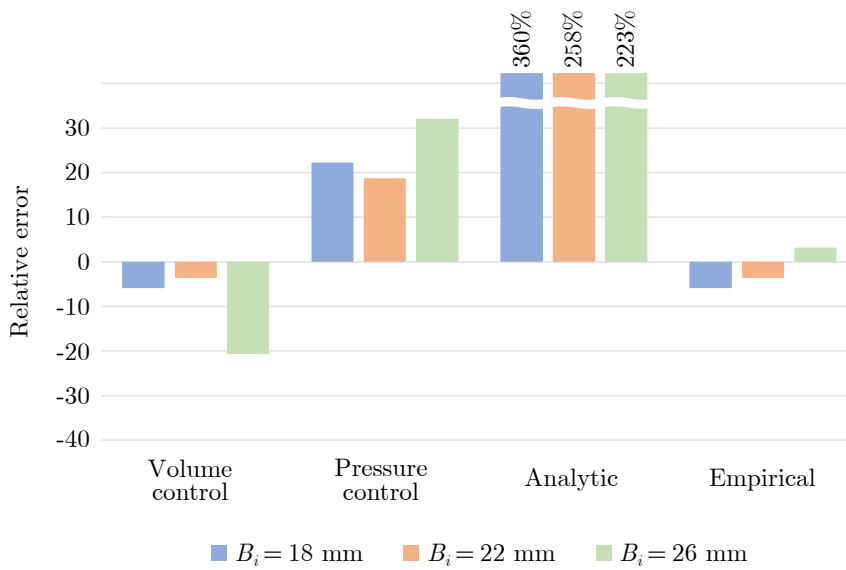


Figure 6.5: Relative error compared to the simulated values

As a consequence of these, **the measurement and calculation methods that were presented are capable of characterizing the snap-through problem** of soft elastic shells, in the considered range of geometries.

7

Summary

7.1 Summary of the paper

The problem of structural stability loss is one of the most critical stages of engineering design. In conventional structures, the aim is to avoid instability problems as safely as possible. However, these instabilities can be exploited for structures made of the right material and with the right geometry, since the multiple deformation between two stable positions does not imply failure.

In this work, a multidisciplinary study has been carried out, which was centered around the characterization of the snap-through phenomena. The aim was to propose numerical, analytical and measurement methods which are capable of predicting how an elastic shell with a specific geometry will behave during different loading condition.

A tématerületen végzett korábbi munkáim során egy numerikus szimulációs környezet került kialakításra, amely alkalmas az elliptikus héjak viselkedésének elemzésére. Ezt követően egy kísérleti berendezést terveztem és építettem meg, amely a héj által bezárt térfogat felfújásán alapul. Ezzel a kísérleti elrendezéssel a folyadékon keresztül érjük el a héj külső terhelését, így annak átpattanását egyik stabil helyzetéből a másikba. A kísérleti berendezés kereskedelmi forgalomban beszerezhető alkatrészekből épült, különös figyelmet fordítva a berendezés egyszerűségére. A dolgozatban bemutatott harmadik módszer a héjak analitikus modellezése volt.

After the methods has been established, a comparison study has been carried out: three main types of shell geometry was selected and they were tested according to the presented methods. The results proved, that the methods are in good agreement with each other.

Further lines of inquiry are set out in the following ideas:

- a time-dependent study of the snap-through phenomenon,
- more experimental tests, to tune the controller of the fluidic control board,
- derive the analytical theory for this exact material based on *Hill* [30, 31].

7.2. A dolgozat összefoglalója

Az szerkezeti stabilitásvesztés problémája a mérnöki tervezésnek egyik legkritikusabb lépcsőfoka. Hagyományos szerkezeteknél igyekeznek minél nagyobb biztonsággal elkerülni az instabilitási problémákat. Azonban ezen instabilitások a megfelelő anyagból készült, és megfelelő geometriával rendelkező szerkezetek esetén kihasználhatók, mivel a két stabil helyzet közötti sokszoros alakváltozás sem jelent tönkremenetelt.

Dolgozatom során egy több lépcsőfokból álló tanulmányt végeztem el, amelynek középpontjában vékony gumyszerű héjak átpattanási jelensége áll. A dolgozat célja olyan numerikus, analitikus és mérési módszerek felállítása, amelyek képesek előrejelezni egy adott geometriájú rugalmas héj viselkedését különböző terhelési körülmények között.

A fenti módszerek kidolgozása után összehasonlító vizsgálatot végeztem három héjgeometriát kiválasztva. A számítási és mérési eredmények feldolgozása során megfigyelhető volt, hogy a különböző módszerek eredményei jó egyezést mutatnak, amely egyben azt is jelzi, hogy a kidolgozott és bemutatott módszerek képesek lágy, rugalmas héjak ezen stabilitásvesztési problémáját karakterizálni.

További vizsgálati irányokat fogalmaznak meg az alábbi gondolatok:

- az átpattanás jelenségének időbeli vizsgálata,
- több mérési program elvégzése, a mérőberendezés szabályozásának pontosítása,
- analitikus számítások levezetése *Hill* nyomán [30, 31].

References

- [1] Carmel Majidi. “Soft Robotics: A Perspective - Current Trends and Prospects for the Future”. In: *Soft Robotics* 1.1 (Mar. 2014), pp. 5–11.
- [2] Deepak Trivedi, Christopher D. Rahn, William M. Kier, and Ian D. Walker. “Soft robotics: Biological inspiration, state of the art, and future research”. In: *Applied Bionics and Biomechanics* 5.3 (Dec. 2008), pp. 99–117.
- [3] Wang Zheng, Polygerinos Panagiotis, and Alazmani Ali. *Soft robotics toolkit; accessed at: 2023. 10. 31*. URL: <https://softroboticstoolkit.com/>.
- [4] Zoelly Robert. “Ueber ein Knickungsproblem an der Kugelschale”. de. PhD thesis. 1915.
- [5] Szabolcs Berezvai. “Constitutive modelling of compressible solids including viscoelastic-viscoplastic effects”. PhD thesis. Budapest University of Technology and Economics, 2020.
- [6] Gerhard A. Holzapfel. *Nonlinear solid mechanics. A continuum approach for engineering*. Repr. Literaturverz. S. 415 - 434. Chichester: Wiley, 2010. 455 pp. ISBN: 9780471823193.
- [7] Jörgen Bergstrom. *Mechanics of solid polymers. Theory and computational modeling*. First edition. Includes bibliographical references and index. Amsterdam: William Andrew is an imprint of Elsevier, 2015. 1509 pp. ISBN: 9780323322966.
- [8] Dassault Systèmes. *Abaqus version 6.20*. 2020.
- [9] Aniket Pal, Vanessa Restrepo, Debkalpa Goswami, and Ramses V. Martinez. “Exploiting Mechanical Instabilities in Soft Robotics: Control, Sensing, and Actuation”. In: *Advanced Materials* 33.19 (Mar. 2021).
- [10] Johannes T. B. Overvelde, Tamara Kloek, Jonas J. A. D’haen, and Katia Bertoldi. “Amplifying the response of soft actuators by harnessing snap-through instabilities”. In: *Proceedings of the National Academy of Sciences* 112.35 (Aug. 2015), pp. 10863–10868.
- [11] Yichao Tang, Yinding Chi, Jiefeng Sun, Tzu-Hao Huang, Omid H. Maghsoudi, Andrew Spence, Jianguo Zhao, Hao Su, and Jie Yin. “Leveraging elastic instabilities for amplified performance: Spine-inspired high-speed and high-force soft robots”. In: *Science Advances* 6.19 (May 2020).

- [12] Zechen Xiong, Yufeng Su, and Hod Lipson. *Fast Untethered Soft Robotic Crawler with Elastic Instability*. 2022.
- [13] E. Riks. “An incremental approach to the solution of snapping and buckling problems”. In: *International Journal of Solids and Structures* 15.7 (1979), pp. 529–551.
- [14] M.A. Crisfield. “A fast incremental/iterative solution procedure that handles snap-through”. In: *Computers & Structures* 13.1-3 (June 1981), pp. 55–62.
- [15] Nan Hu and Rigoberto Burgueño. “Buckling-induced smart applications: recent advances and trends”. In: *Smart Materials and Structures* 24.6 (May 2015), p. 063001.
- [16] Xinjie Zhang, Ayobami Elisha Oseyemi, Ke Ma, and Shouyi Yu. “Entirely soft valve leveraging snap-through instability for passive flow control”. In: *Sensors and Actuators B: Chemical* 367 (Sept. 2022), p. 132035.
- [17] E.B. van der Houwen, L.H. Kuiper, J.G.M. Burgerhof, B.F.A.M. van der Laan, and G.J. Verkerke. “Functional buckling behavior of silicone rubber shells for biomedical use”. In: *Journal of the Mechanical Behavior of Biomedical Materials* 28 (Dec. 2013), pp. 47–54.
- [18] Ying Lin, Yi-Xian Xu, and Jia-Yang Juang. “Single-Actuator Soft Robot for In-Pipe Crawling”. In: *Soft Robotics* 10.1 (Feb. 2023), pp. 174–186.
- [19] Benjamin Gorissen, David Melancon, Nikolaos Vasios, Mehdi Torbati, and Katia Bertoldi. “Inflatable soft jumper inspired by shell snapping”. In: *Science Robotics* 5.42 (May 2020).
- [20] Anna Lee, Francisco López Jiménez, Joel Marthelot, John W. Hutchinson, and Pedro M. Reis. “The Geometric Role of Precisely Engineered Imperfections on the Critical Buckling Load of Spherical Elastic Shells”. In: *Journal of Applied Mechanics* 83.11 (Sept. 2016).
- [21] Jose Barreiros, Houston Claire, Bryan Peele, Omer Shapira, Josef Spjut, David Luebke, Malte Jung, and Robert Shepherd. “Fluidic Elastomer Actuators for Haptic Interactions in Virtual Reality”. In: *IEEE Robotics and Automation Letters* 4.2 (Apr. 2019), pp. 277–284.
- [22] Arefeh Abbasi, Dong Yan, and Pedro M. Reis. “Probing the buckling of pressurized spherical shells”. In: *Journal of the Mechanics and Physics of Solids* 155 (Oct. 2021), p. 104545.
- [23] D. Karagiozova, X. -W. Zhang, and T. -X. Yu. “Static and dynamic snap-through behaviour of an elastic spherical shell”. In: *Acta Mechanica Sinica* 28.3 (June 2012), pp. 695–710.
- [24] Wacker Chemical Corporation. *Elastostil M4061 A/B*; accessed at: 2023. 11. 01. URL: <https://bit.ly/elastostil-m-4061-ab>.
- [25] Stephen P. Timoshenko. *Theory of elastic stability*. Ed. by James M. Gere. Second edition. EBL-Schweitzer. Description based upon print version of record. Newburyport: Dover Publications, 2012. 11067 pp. ISBN: 9780486134802.

- [26] Th. von Karman and Hsue-Shen Tsien. “The Buckling of Spherical Shells by External Pressure”. In: *Journal of the Aeronautical Sciences* 7.2 (Dec. 1939), pp. 43–50.
- [27] R. L. Carlson, R. L. Sendelbeck, and N. J. Hoff. “Experimental studies of the buckling of complete spherical shells”. In: *Experimental Mechanics* 7.7 (July 1967), pp. 281–288.
- [28] K. Tao S. Taeprasartsit. “Effect of shell geometry and material constants on dynamic buckling load of elastic perfect clamped spherical caps”. In: *Asian Journal of Civil Engineering* (2005).
- [29] Wendell B. Stephens and Robert E. Fulton. “Axisymmetric static and dynamic buckling of spherical caps due to centrally distributed pressures”. In: *AIAA Journal* 7.11 (Nov. 1969), pp. 2120–2126.
- [30] James M. Hill. “Buckling of long thick-walled circular cylindrical shells of isotropic incompressible hyperelastic materials under uniform external pressure”. In: *Journal of the Mechanics and Physics of Solids* 23.2 (Apr. 1975), pp. 99–112.
- [31] James M. Hill. “Critical pressures for the buckling of thick-walled spherical shells under uniform external pressure”. In: *The Quarterly Journal of Mechanics and Applied Mathematics* 29.2 (1976), pp. 179–196.

The coordinates of each point can be easily obtained in the y direction using the opening angles and the radii, but in the x direction we need to calculate the intersection points of primitive geometric shapes, such as circles, ellipses, and lines. The x coordinate of the first four points is zero because these are laying on the axis of rotation. Their y coordinate can be easily obtained using the parameters B_i , R_o , and the shells' thickness. The first intersection point which needs to be calculated is the x coordinate of the point P_5 , which can be constructed using the intersection (is. in further readings) of a circle and a line, such as:

$$x^2 + (y - \Delta)^2 = \left(R_o + \frac{t_o}{2}\right)^2 \quad \text{circle and the } y = \Delta + R_o \cos \theta_o \quad \text{line is.} \quad (\text{A.1})$$

from which the x coordinate is expressed by substituting the second equation into the first:

$$x_5 = \sqrt{\left(R_o + \frac{t_o}{2}\right)^2 - (R_o \cos \theta_o)^2}. \quad (\text{A.2})$$

Point P_6 can be written in terms of the inner and the outer cap's parameters as well. First, the outer cap's circle and The point P_6 can be described by the geometric parameters of both the inner and outer shells. First, considering the outer shell, we look for the intersection of a circle and a line in the form:

$$x^2 + (y - \Delta)^2 = \left(R_o - \frac{t_o}{2}\right)^2 \quad \text{circle and the } y = \Delta + R_o \cos \theta_o \quad \text{line is.} \quad (\text{A.3})$$

from which the x coordinate:

$$x_6^o = \sqrt{\left(R_o - \frac{t_o}{2}\right)^2 - (R_o \cos \theta_o)^2}. \quad (\text{A.4})$$

The same point with respect to the inner cap's parameters as:

$$\frac{x^2}{\left(A_i + \frac{t_i}{2}\right)^2} + \frac{y^2}{\left(B_i + \frac{t_i}{2}\right)^2} = 1 \quad \text{ellipse and the } y = r_e \cos \theta_i \quad \text{line is.} \quad (\text{A.5})$$

from which the x coordinate can be obtained as:

$$x_6^i = \sqrt{\left(1 - \frac{r_e^2 \cos^2 \theta_i}{\left(B_i + \frac{t_i}{2}\right)^2}\right) \cdot \left(A_i + \frac{t_i}{2}\right)^2}, \quad (\text{A.6})$$

where r_e is the length of the line drawn from the origin to an arbitrary point on the ellipse defined by the opening angle θ_i . The formula can be obtained from the polar coded description of the ellipse, given as

$$r_e = \frac{A_i B_i}{\sqrt{A_i^2 \sin^2 \left(\frac{\pi}{2} - \theta_i\right) + B_i^2 \cos^2 \left(\frac{\pi}{2} - \theta_i\right)}}, \quad (\text{A.7})$$

which can be interpreted using the figure below:

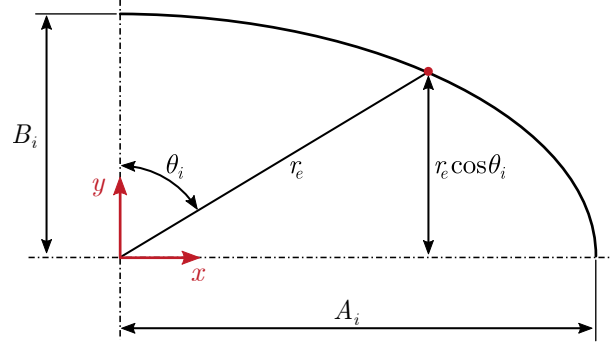


Figure A.2: Interpreting the length of the vector pointing to a given point on the ellipse

The coordinates of points P_7 and P_8 can be easily calculated using the radius and thickness of the ring, respectively, thus they are not discussed in detail. Finally, the point P_9 is defined by

$$\frac{x^2}{\left(A_i - \frac{t_i}{2}\right)^2} + \frac{y^2}{\left(B_i - \frac{t_i}{2}\right)^2} = 1 \quad \text{ellipse and the } y = r_e \cos \theta_i - t_r \quad \text{line is.} \quad (\text{A.8})$$

from which the x coordinate:

$$x_9 = \sqrt{\left(1 - \frac{(r_e \cos \theta_i - t_r)^2}{\left(B_i - \frac{t_i}{2}\right)^2}\right) \cdot \left(A_i - \frac{t_i}{2}\right)^2}. \quad (\text{A.9})$$

Using the notations shown in Fig. A.1 and the derivations, the coordinates of each point are summarized below:

$$P_1 = \left(0, B_i - \frac{t_i}{2}\right), \quad (\text{A.10})$$

$$P_2 = \left(0, B_i + \frac{t_i}{2}\right), \quad (\text{A.11})$$

$$P_3 = \left(0, \Delta + B_i - \frac{t_o}{2}\right), \quad (\text{A.12})$$

$$P_4 = \left(0, \Delta + B_i + \frac{t_o}{2}\right), \quad (\text{A.13})$$

$$P_5 = \left(\sqrt{\left(R_o + \frac{t_o}{2}\right)^2 - (R_o \cos \theta_o)^2}, \Delta + R_o \cos \theta_o\right), \quad (\text{A.14})$$

$$P_6^i = \left(\sqrt{\left(1 - \frac{r_e^2 \cos^2 \theta_i}{\left(B_i + \frac{t_i}{2}\right)^2}\right) \cdot \left(A_i + \frac{t_i}{2}\right)^2}, r_e \cos \theta_i\right), \quad (\text{A.15})$$

$$(\text{A.16})$$

$$P_6^o = \left(\sqrt{\left(R_o - \frac{t_o}{2}\right)^2 - (R_o \cos \theta_o)^2}, \Delta + R_o \cos \theta_o \right), \quad (\text{A.17})$$

$$P_7 = (R_r, r_e \cos \theta_i), \quad (\text{A.18})$$

$$P_8 = (R_r, r_e \cos \theta_i - t_r), \quad (\text{A.19})$$

$$P_9 = \left(\sqrt{\left(1 - \frac{(r_e \cos \theta_i - t_r)^2}{(B_i - \frac{t_i}{2})^2}\right) \cdot \left(A_i - \frac{t_i}{2}\right)^2}, r_e \cos \theta_i - t_r \right). \quad (\text{A.20})$$

However, an enclosed volume is formed only if the outer and inner shells are in contact at point P_6 , so the following expressions must hold:

$$x_6^i = x_6^o \quad \text{and} \quad y_6^i = y_6^o. \quad (\text{A.21})$$

By comparing the y coordinates of (A.15) and (A.16), the distance between the center of the ellipse and the center of the circle can be expressed as

$$\Delta = r_e \cos(\theta_i) - R_o \cos(\theta_o). \quad (\text{A.22})$$

Similarly, by comparing the x coordinates, we can conclude that the radius of the outer shell can be expressed by the following quadratic equation:

$$R_o = \frac{-B \pm \sqrt{(B^2 - 4AC)}}{2A}, \quad (\text{A.23})$$

where the coefficients are given by

$$A = 1 - \cos^2 \theta_o, \quad (\text{A.24})$$

$$B = -t_o, \quad (\text{A.25})$$

$$C = \frac{t_o^2}{4} - (x_6^i)^2. \quad (\text{A.26})$$

The conclusion is that the distance between the centers of the two shapes and the radius of the outer shell are not independent parameters, they can be described using a function in terms of the other parameters. It is important to note that Eq. (A.23) has two solutions in general. The larger of the two should always be chosen, to ensure that the geometry and the following calculations are correct. To ensure that the inflatable cavity is created, we can use the constraint equations

$$y_2 < y_3 \quad \text{and} \quad \theta_i < \theta_o \quad (\text{A.27})$$

which needs to be satisfied for each combination of the parameters. The coordinates of the points defining the geometry can be easily calculated using a PYTHON script, which first calculates the radius according to Eq. (A.23), which is then used to calculate the center-to-center distance expressed in Eq. (A.22). The program then computes all coordinates, taking into account the constraint equations introduced in Eq. (A.27). Of course, the ring's radius (R_r) and thickness (t_r), the outer shell's opening angle (θ_o) and thickness (t_o) must be defined too, but for the sake of simplicity, I do not treat them as input parameters, instead, I calculate them by creating relations to the rest of the geometry (because their values are not so determinant). The opening angle is chosen to be $\theta_o = 90^\circ$ for all of the simulations. The geometric relations can be expressed such as the radius of the ring must be bigger than the coordinate x_5 , thus

$$R_r = x_5 + 0,05 \cdot x_5 = 1,05 \cdot x_5. \quad (\text{A.28})$$

The thicknesses are defined by the following expression:

$$t_r = t_o = \frac{t_i}{2}. \quad (\text{A.29})$$

Using these assumptions, the axisymmetric geometry is defined using 4 input parameters, which are used to describe the inner elliptical shell in its entirety. These parameters are the semi-axes (A_i and B_i), the opening angle (θ_i) and the shell's thickness (t_i).

B

Finite element modelling

B.1 Mesh independence study

A mesh independence study was carried out to ensure that the discretization is fine enough. The used model does not differ from the ones that were introduced, only the mesh size was changed. The model can be seen on the figure below, which has a geometric properties of:

$$A_i = 22 \text{ mm}, \quad B_i = 18 \text{ mm}, \quad t_i = 2.5 \text{ mm} \quad \theta_i = 65^\circ. \quad (\text{B.1})$$

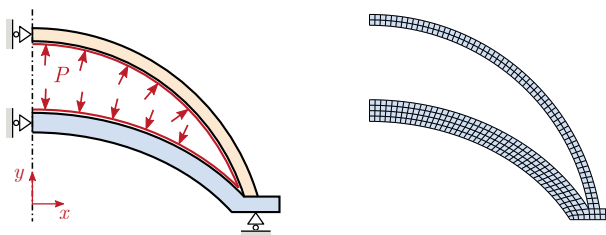


Figure B.1: The finite element model (left) with a coarse mesh (right)

The mesh size is automatically calculated by a program code, with the assumption, that the outer shell (which has a thickness of $t_o = t_i/2$) is divided into M number of elements ($M \in \mathbb{N}^+$). Three cases were investigated, starting from $M = 2$, then $M = 4$ and eventually reaching $M = 8$.

The resulting pressure - volume curve from the model discretized with the finest element size ($M = 8$) can be seen on the left of Fig. B.2. If we plot the relative error between the

$M8 - M4$ and the $M8 - M2$ case, we can create a diagram which can be seen on the right hand side of Fig. B.2. Taking a closer look, we can see that even the biggest difference was around 2.2% between the $M8$ and $M4$ case (even in the case of $M8$ and $M2$ this maxima is around 3.1%), which is negligible in the case of the original pressure range.

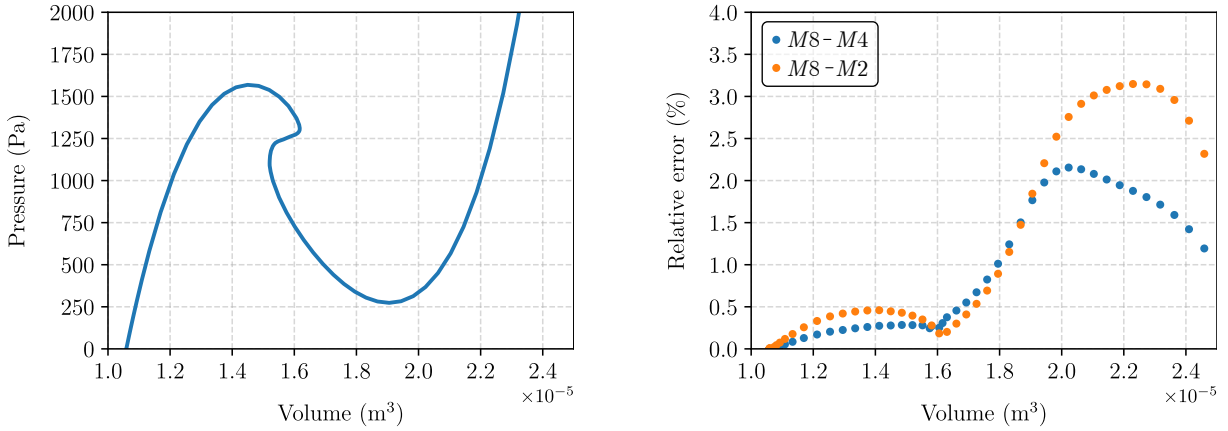


Figure B.2: The resulting pressure-volume curve from the finest mesh (left) and the relative errors between the meshes (right)

As a consequence of this, we can be sure that our numerical calculations will be independent of the mesh size, if we use the $M = 4$ division rule for all of our models.

B.2 Deformation of the measurement container

This section of the appendix contains a short study of the measurement container which is made out of ABS, to prove that the occurring pressures does not deform it significantly.

The boundary conditions (fixed support at the bottom) and the loading by the pressure ($P = 20$ kPa, which is beyond the expected range for the shells) can be seen on the figure below. The mesh size was appropriately fine enough, and the results stated that the maximum deformation of the container is around 0.09 mm.

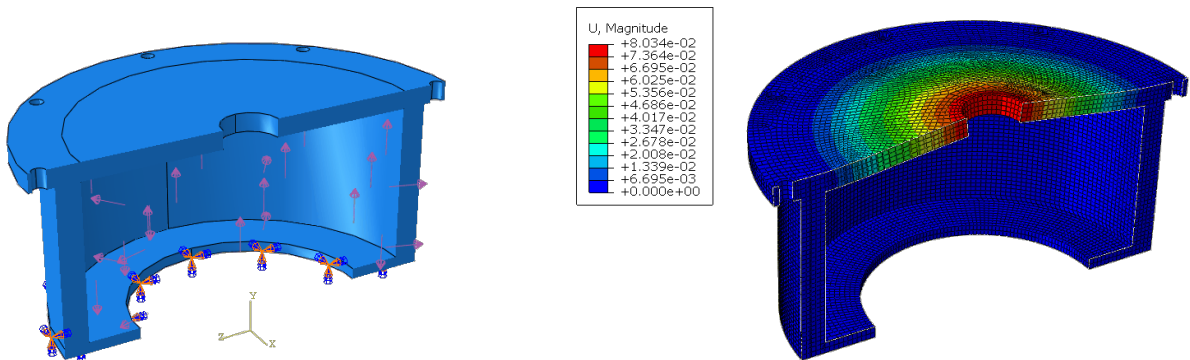


Figure B.3: The boundary conditions and the results (deformation magnified by 50)

The material properties for the ABS was determined as $E = 2.04$ GPa, $\nu = 0.37$ and $\rho = 1040$ kg/m³ based on *MatWeb*.

C

Characteristic of the used diaphragm pump

The characteristic of the diaphragm pump is defined by a voltage-volume flow rate curve. We can create a simple measurement setup, to deduct this relationship as follows:

1. Set up a range of voltage inputs: 5, 6, ... 12 (V), note that the pump cant operate below 5 V of input voltage.
2. Operate the pump for one minute for each input, and measure the volume of the fluid at the destination vessel.
3. Graph the correlation between these.

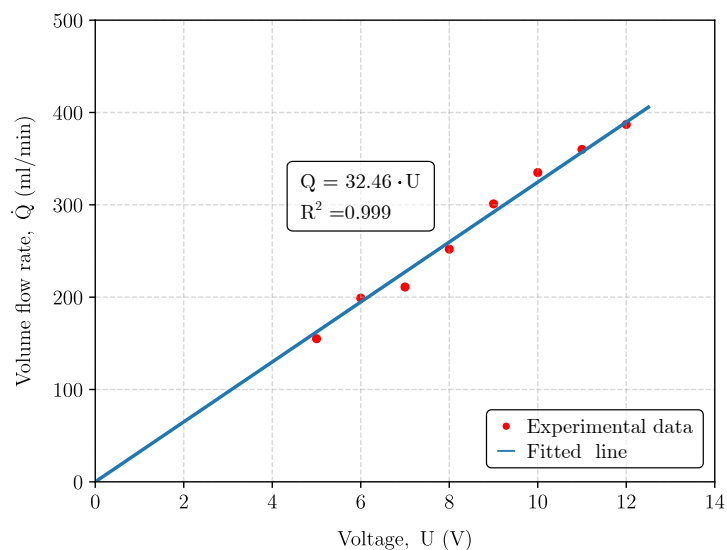


Figure C.1: The linear pump characteristic

D

Optimization script for the equivalent circle

```
1 import numpy as np
2 import matplotlib.pyplot as plt
3 from scipy.optimize import curve_fit
4
5 # Parameters of the elliptical segment
6 A_ell = 22.0 # Semi - major axis
7 B_ell = 18.0 # Semi - minor axis
8 Q_ell = np.radians(60.0) # Opening angle
9
10 # Function to calculate the points of the elliptical segment
11 def ELLIPSEpoints(A,B,Q):
12     t = np.linspace(np.pi/2-Q, np.pi/2+Q, 1000)
13
14     x = A * np.cos(t) # x coordinate
15     y = B * np.sin(t) # y coordinate
16
17     return x, y
18
19 # Function to calculate the radius of ellipse at a point defined by Q
20 def ELLIPSEradius(A,B,Q):
21     S = np.sin(np.pi/2-Q)
22     C = np.cos(np.pi/2-Q)
23
24     r = A*B/np.sqrt(A**2*S**2 + B**2*C**2)
25
26     return r
27
28 # Function to calculate the points of the circular segment
29 def CIRCLEpoints(ellipse_x,delta,R):
30     x = ellipse_x
31     y = []
32
33     for i in range(len(x)):
34         yc = delta + np.sqrt(R**2 - x[i]**2)
35         y.append(yc)
36
37     return y
```

```

38
39 # Function to calculate the points of the circular segment with the obtained values
40 def CIRCLEobtained(R,delta,Q):
41     t = np.linspace(np.pi/2-Q, np.pi/2+Q, 1000)
42     x = R * np.cos(t)
43     y = R * np.sin(t) + delta
44
45     return x, y
46
47 # The elliptical segment
48 x_ell, y_ell = ELLIPSEpoints(A_ell, B_ell, Q_ell)
49
50 # Find the best fitting circle with the initial guess of p0 = [delta, R]
51 constants = curve_fit(CIRCLEpoints, x_ell, y_ell, p0=[-2, 22])
52 delta_cir = round(constants[0][0], 5)
53 R_cir = round(constants[0][1], 5)
54
55 # Find the opening angle of the circle by the law of sines
56 R_ell = ELLIPSEradius(A_ell, B_ell, Q_ell)
57 Q_cir = np.arcsin(R_ell/R_cir*np.sin(np.pi-Q_ell))
58
59 # Print the obtained values
60 print(f'The obtained parameters of the equivalent circle:\n* R = {R_cir} [mm],\n*
61       Q_cir = {round(np.degrees(Q_cir), 3)} deg.')
62
63 # The circular segment
64 x_cir, y_cir = CIRCLEobtained(R_cir,delta_cir,Q_cir)
65
66 # Plot the ellipse and the circle
67 plt.figure()
68
69 plt.plot(x_ell, y_ell, linewidth=2)
70 plt.plot(x_cir, y_cir, linewidth=2)
71 plt.scatter(0, 0, s=10, color='C0')
72 plt.scatter(0, delta_cir, s=10, color='C1')
73
74 plt.legend(labels=['Ellipse', 'Circle'])
75 plt.xlim(-A_ell*1.5, A_ell*1.5)
76 plt.ylim(delta_cir*1.5, B_ell*1.5)
77 plt.gca().set_aspect('equal', adjustable='box')
78 plt.title('Comparison')
79 plt.xlabel('X')
80 plt.ylabel('Y')
81 plt.grid()
82 plt.savefig('test.pdf')
83 plt.show()

```